Numerical Uncertainties in the Simulation of Reversible Isentropic Processes and Entropy Conservation

DONALD R. JOHNSON

Space Science and Engineering Center, Cooperative Institute for Meteorological Satellite Studies, and Department of Atmospheric and Oceanic Sciences, University of Wisconsin—Madison, Madison, Wisconsin, and Division of Earth Sciences, Universities Space Research Association, Columbia, Maryland

ALLEN J. LENZEN

Space Science and Engineering Center, University of Wisconsin—Madison, Madison, Wisconsin

TOM H. ZAPOTOCNY

Space Science and Engineering Center, and Cooperative Institute for Meteorological Satellite Studies, University of Wisconsin—Madison, Madison, Wisconsin

TODD K. SCHAACK

Space Science and Engineering Center, University of Wisconsin—Madison, Madison, Wisconsin

(Manuscript received 4 December 1998, in final form 31 August 1999)

ABSTRACT

A challenge common to weather, climate, and seasonal numerical prediction is the need to simulate accurately reversible isentropic processes in combination with appropriate determination of sources/sinks of energy and entropy. Ultimately, this task includes the distribution and transport of internal, gravitational, and kinetic energies, the energies of water substances in all forms, and the related thermodynamic processes of phase changes involved with clouds, including condensation, evaporation, and precipitation processes.

All of the processes noted above involve the entropies of matter, radiation, and chemical substances, conservation during transport, and/or changes in entropies by physical processes internal to the atmosphere. With respect to the entropy of matter, a means to study a model's accuracy in simulating internal hydrologic processes is to determine its capability to simulate the appropriate conservation of potential and equivalent potential temperature as surrogates of dry and moist entropy under reversible adiabatic processes in which clouds form, evaporate, and precipitate. In this study, a statistical strategy utilizing the concept of ''pure error'' is set forth to assess the numerical accuracies of models to simulate reversible processes during 10-day integrations of the global circulation corresponding to the global residence time of water vapor. During the integrations, the sums of squared differences between equivalent potential temperature θ_e numerically simulated by the governing equations of mass, energy, water vapor, and cloud water and a proxy equivalent potential temperature $t\theta_e$ numerically simulated as a conservative property are monitored. Inspection of the differences of θ_e and $t\theta_e$ in time and space and the relative frequency distribution of the differences details bias and random errors that develop from nonlinear numerical inaccuracies in the advection and transport of potential temperature and water substances within the global atmosphere.

A series of nine global simulations employing various versions of Community Climate Models CCM2 and CCM3—all Eulerian spectral numerics, all semi-Lagrangian numerics, mixed Eulerian spectral, and semi-Lagrangian numerics—and the University of Wisconsin—Madison (UW) isentropic-sigma gridpoint model provides an interesting comparison of numerical accuracies in the simulation of reversibility. By day 10, large bias and random differences were identified in the simulation of reversible processes in all of the models except for the UW isentropic-sigma model. The CCM2 and CCM3 simulations yielded systematic differences that varied zonally, vertically, and temporally. Within the comparison, the UW isentropic-sigma model was superior in transporting water vapor and cloud water/ice and in simulating reversibility involving the conservation of dry and moist entropy. The only relative frequency distribution of differences that appeared optimal, in that the distribution remained unbiased and equilibrated with minimal variance as it remained statistically stationary, was the distribution from the UW isentropic-sigma model. All other distributions revealed nonstationary characteristics with spreading and/or shifting of the maxima as the biases and variances of the numerical differences of θ_e and $t\theta_e$ amplified.

Corresponding author address: Dr. Donald R. Johnson, Space Science and Engineering Center, University of Wisconsin—Madison, 1225 W. Dayton Street, Madison, WI 53706.
E-mail: donj@ssec.wisc.edu

1. Introduction

Von Neumann (1960) stated that atmospheric numerical prediction may be represented by three categories: numerical weather prediction based on initial data, climate prediction determined by factors other than the initial state, and intermediate-range prediction for which certain traits of the initial conditions influence the outcome of the prediction. Von Neumann correctly perceived that the easiest problem is numerical weather prediction, the next most difficult problem is climate prediction, and the most difficult is intermediate-range prediction. With the recent advent of seasonal prediction where the initial boundary conditions of oceans are important, atmospheric scientists are now engaged in all three endeavors nearly four decades after von Neumann's remarks. Each of the three categories poses differing challenges. However, one central challenge common to all three is the need to simulate accurately the distribution and transport of water substances in all forms: adiabatic expansion and compression that induce the related thermodynamic processes of phase changes involved with condensation, evaporation, and precipitation processes; the resulting cloudiness; and then the influence of water substances on the flux of radiation and other processes involving hygroscopic aerosols and atmospheric chemistry. In view of the elusive nature of meeting this challenge, an early question that emerges is just what are the barriers that must be surmounted, or alternatively are there insurmountable barriers that limit predictability of these processes? If so, just what are their origins: theoretical, numerical, resolution of observations, and models, etc.?

In all three categories of prediction noted by von Neumann (1960), the accuracy of a model depends in part on its capability to simulate the appropriate conservation of potential and equivalent potential temperature as surrogates for entropies under dry and moist reversible adiabatic processes within which long-range transport is an intrinsic component. The thrust of this study will be to assess the accuracy of global models to simulate reversible processes. This assessment will involve the explicit simulation of the transport of water vapor and cloud water/ice, and cloud condensation/evaporation in conjunction with heating/cooling from phase changes. Results will be presented that contrast bias and random errors from the different models ranging from a few tenths to tens of degrees over a 10-day period. These results will raise the pragmatic issues of ''to what degree is parameterization of diabatic processes used to offset bias and random errors of numerical inconsistencies'' and ''just what are the limits of predictability'' in terms of a model's capability to simulate accurately the entropy balance in relation to hydrologic, radiative, and chemical processes? While these pragmatic issues are not addressed directly in the studies to be presented, the statistical strategies set forth are directed to these matters.

For the most part, the success of medium-range weather prediction models has been determined from verification against the final analysis, and statistical analyses involving anomaly correlation, rms errors, precipitation patterns, etc. Likewise for the most part the success of climate models has been judged from comparisons of the temporally, zonally, and sometimes vertically or horizontally averaged simulated states against corresponding averaged observed data or assimilated states with attention being given to temperature and other state structure. All of these depend on observational capabilities in time and space, data assimilation, and the corresponding models employed in data assimilation. For understandable reasons only limited attention has been devoted to internal processes involved with source/sink functions of dependent properties and/or long-range transport of dry static, latent, and sensible energies, etc. Sources and sinks of energy by differential heating and momentum by pressure/viscous stresses are not directly observable, nor are there means to assess inaccuracies in the nonlinearity of transport. The importance of the entropy balance in relation to both its structure, its exchange, and its sources and sinks has received almost no attention in both medium-range weather prediction and climate modeling.

Emphasis has been given to the entropy principle in computational fluid dynamics, although within a different context. With roots tracing to the works of von Neumann (1943) and Lax (1971), Merriam's (1989) emphasis is on the suppression of nonlinear instability through sources of entropy by numerical diffusion. Hughes et al. (1986) show that with the addition of heat diffusion and viscous dissipation in the governing equations the mathematical definition of entropy introduced for the compressible Euler equations reduces to the classic definition of entropy defined through the second law of thermodynamics. Within atmospheric science, Arakawa and Lamb (1977) have emphasized the relevance of conservation of entropy and its surrogate potential temperature. More recently Egger (1999) has studied entropy conservation for a family of numerical algorithms. From the authors' viewpoint, the key challenge in overcoming the limitations imposed by the entropy principle globally is to minimize the numerical diffusion of dry static energy and water vapor that is intrinsic to vertical advection of properties. Extreme vertical gradients of trace constituents including water vapor are generated through baroclinic instability by the strong horizontal and vertical wind shear within the westerly wind regime. The resulting structure in combination with frontal deformation, rotation, and vertical advection leads to numerical difficulties.

Although outwardly there is a certain degree of redundancy in directing attention to both entropy and energy, there are fundamental differences (Johnson 1989, 1997, 2000) that are directly related to advancing predictability for both weather prediction and climate models. Entropy is a fundamental extensive property whose

changes only occur through differential heating. Entropy unlike energy is not transformed by isentropic processes within the atmosphere. There is also the key role of entropy in the definition of potential vorticity as it constrains the stretching or shrinking of vortex tubes within a stratified atmosphere. Thus from both dynamical and physical principles a first-order consideration in the accuracy of simulated weather and climate states should be directed to entropy, its sources/sinks and the model's capability to simulate reversible isentropic processes accurately, including those associated with clouds and condensation/evaporation in the free atmosphere. As Sommerfeld (1964, p. 19) states, ''in spite of their not being real, isentropic processes are most important in thermodynamics because definite equations can only be obtained by considering reversible changes.'' One may add that models must be able to simulate reversible processes accurately since in the maintenance of atmospheric circulation against dissipation the transformation of potential and kinetic energy occurs through reversible processes.

An accurate simulation of reversibility requires within the marching problem, that mass, dry static energy, water vapor, and cloud water be advected and/or transported consistently by the four independent but physically coupled nonlinear governing equations for these properties, such that the surrogate for moist entropy θ_e as a derived property is appropriately conserved in the Lagrangian sense. Basically, numerical errors in the simulation of a given property stem from truncation or rounding. Then compounding of numerical errors occurs from the need to simulate conservation of derived properties like θ_e, potential vorticity, and chemical substances, all of which depend on combining the predictions of the individual nonlinear predictive equations of the model itself. For example, differing truncation errors from the differing patterns of atmospheric properties and also different numerical algorithms leads to inconsistencies in simulating conservation of dry and/or moist entropy. While all error forms degrade numerical solutions, ideally the aim is to simulate weather and climate states within which the differing truncation and rounding errors of the coupled nonlinear finite difference equations do not interact with each other and the true state and thus further degrade prediction of future states with respect to simulating reversibility.

Within an overall aim to establish from empirical evidence that aphysical sources of entropy exist in weather and climate models as a complement to Johnson's (1997) earlier analysis, two objectives of this study are now stated. The objectives are 1) to set forth useful strategies to examine the capability of models to simulate reversibility, and 2) to examine the magnitude of errors in the simulation of reversible processes in relation to numerical inconsistencies and aphysical sources of entropy in weather and climate models.

The strategy set forth employs statistical concepts to estimate ''pure error from replicated observations'' (Anderson and Bancroft 1952; Box et al. 1978). Furthermore, the strategy focuses on the analysis of both the state structure of the errors in time and space and their statistical description in order to isolate bias from random components and, in turn, relate bias to physical aspects of the simulation. As the first example of the application of the strategy to assess pure error, the capabilities for simulating reversible processes in the University of Wisconsin—Madison (UW) hybrid isentropic-sigma (θ–σ) model and in the National Center for Atmospheric Research (NCAR) Community Climate Models CCM2 and CCM3 will be compared in detail. Within NCAR's series of CCMs that have been developed, the underlying numerical methods have shifted from employing an Eulerian representation of the governing equations in combination with spectral methods to semi-Lagrangian methods. NCAR's CCM2 and CCM3 actually use a combination of Eulerian spectral numerics for mass, momentum, and enthalpy equations and semi-Lagrangian numerics for water vapor and other trace constituents. After the detailed statistical comparison of the UW θ–σ model and CCM3, the results from three follow-on experiments are included to gain insight into the relative accuracies of simulation of reversible processes by different combination of numerical algorithms.

2. Assessing numerical accuracies in the simulation of reversibility

In earlier studies Zapotocny et al. (1996, 1997a,b) studied the capabilities of several global models to conserve appropriately equivalent potential temperature and potential vorticity, and also the extrema of an idealized trace constituent over periods of 10 days under isentropic conditions. Under the idealized dry isentropic conditions, the governing equations for the atmospheric continuum require the joint distributions of the appropriate atmospheric property and its proxy to be conserved. The sum of the squares of the deviations between the property and its proxy provide an objective measure of a model's skill to conserve the joint distributions. Skill in ensuring conservation decreases as the magnitudes of numerical errors and inconsistencies among the coupled nonlinear governing equations for thermodynamics increase.

The underlying logic now is to extend these earlier studies to the more difficult challenge of simulating reversibility through ascertaining the accuracy of a model to conserve moist entropy. Statistical analyses will be employed to isolate random and systematic components of the numerical inaccuracies including the temporal rate of error growth. Furthermore, the statistical methods can be applied more generally to study conservation of various properties. The properties to be considered are dry entropy, moist entropy, water vapor, trace constituents, aerosols, potential vorticity, and their sources and sinks. Under dry isentropic processes and source-free

transport all are conserved, while under moist reversible processes and source-free transport, only the moist entropy, trace constituents, and aerosols are conserved.

The strategy for this assessment will be based on examining how well the joint distributions of an atmospheric property (f) and its counterpart proxy (tf) are conserved relative to each other under stated conditions where the counterpart proxy is governed by a continuity equation appropriate to a trace constituent. For example, if the proxy field of equivalent potential temperature $t\theta_e$ corresponds identically at an initial time to the actual field θ_e and the governing equations are simplified to represent moist reversible isentropic processes, the continuum equations demand that the two fields should remain identical, that is, the state conditions for θ_e and $t\theta_e$ retain a one-to-one correspondence at all information points in the model. In this case, the evolution of θ_e is determined by the coupled nonlinear governing equations for mass, energy, water vapor, and cloud water/ice, while the evolution of $t\theta_e$ is determined solely from a source-free continuity equation. Within the governing equations, both θ_e and $t\theta_e$ have common dependence on the mass transport $\rho J_\eta \mathbf{U}$ with its evolution being governed by the model's equations of motion. [Here J_η as $|\partial z/\partial \eta|$ transforms the vertical coordinate geopotential height to the generalized vertical coordinate η (Johnson 1980).] Since the model's state variables are defined by a discrete set of grid points and/or spectral coefficients within the set of equations determining temporal evolution, spurious numerical diffusion/dispersion induces differences between the two fields of θ_e and $t\theta_e$. It follows that there is increased opportunity for the development of errors nonlinearly from numerical diffusion/dispersion of the property θ_e since there are four distinct coupled nonlinear equations governing this derived property while the proxy $t\theta_e$ is determined by the single continuity equation. The rate at which the fields θ_e and $t\theta_e$ differ with time provides information on the degree and growth of error from the differing truncation and rounding errors and numerical inconsistencies that are inherent from the discreteness of the four coupled nonlinear and trace continuity equations.

3. Pure error and numerical inaccuracies

By definition the pure error sums of squares (SS) from weighted differences of a model's predicted property (y_i) and its proxy (z_i) is defined by

$$\mathrm{SS} = \sum w_i (y_i - z_i)^2, \tag{1}$$

where the index $i = 1, 2, \ldots, N$ denotes the ith information point and N is the total number of information points. The model's predicted property and its proxy with each defined as the sum of a true value (η_i, ζ_i) and bias (δ_{y_i}, δ_{z_i}) and random (ε_{y_i}, ε_{z_i}) error components are expressed by

$$y_i = \eta_i + \delta_{y_i} + \varepsilon_{y_i}, \tag{2}$$

$$z_i = \zeta_i + \delta_{z_i} + \varepsilon_{z_i}. \tag{3}$$

With the predicted property and its proxy expressed in specific units, weighting recognizes that the specific property must be multiplied by the mass $(\rho J_\eta dA d\eta)_i$ within the ith grid volume in order to determine the total property within the ith grid volume. For simplification the individual weights are determined by dividing the mass in the ith volume element by the total mass of the analysis domain. Thus, the ith weight for the entire model domain as the fractional mass of the given domain is defined by

$$w_i = (\rho J_\eta dA d\eta)_i \Big/ \sum (\rho J_\eta dA d\eta)_j, \tag{4}$$

where ρ is the density, J_η is $|\partial z/\partial \eta|$, and η as the generalized vertical coordinate (Johnson 1980) is a monotonically increasing or decreasing function of height z and j is a dummy index used in summation over the entire domain. In the situation where the analysis domain is a two-dimensional quasi-horizontal layer of a model with uniform $\Delta\eta$, the ith weight reduces to

$$w_i = (\rho J_\eta dA)_i \Big/ \sum (\rho J_\eta dA)_j. \tag{5}$$

Note that summation of the product $w_i y_i$ and also $w_i z_i$ yields the mean of y_i and z_i expressed in specific units.

The substitution of (2) and (3) into (1) yields

$$\mathrm{SS} = \sum w_i [(\eta_i + \delta_{y_i} + \varepsilon_{y_i}) - (\zeta_i + \delta_{z_i} + \varepsilon_{z_i})]^2. \tag{6}$$

Under the assumption for the true state that η_i equal ζ_i for all i, (6) becomes

$$\mathrm{SS} = \sum w_i [(\delta_{y_i} - \delta_{z_i}) + (\varepsilon_{y_i} - \varepsilon_{z_i})]^2 \tag{7}$$

$$= \sum w_i [(\delta_{y_i} - \delta_{z_i})^2 + 2(\delta_{y_i} - \delta_{z_i})(\varepsilon_{y_i} - \varepsilon_{z_i}) + (\varepsilon_{y_i}^2 - 2\varepsilon_{y_i}\varepsilon_{z_i} + \varepsilon_{z_i}^2)]. \tag{8}$$

The expected value of the sums of squares is

$$E(\mathrm{SS}) = \sum w_i \{(\delta_{y_i} - \delta_{z_i})^2 + [E(\varepsilon_{y_i})^2 - 2E(\varepsilon_{y_i}\varepsilon_{z_i}) + E(\varepsilon_{z_i})^2]\}. \tag{9}$$

The four components of the expected value of the pure error sums of squares are the square of the difference of the bias errors for y_i and z_i for all incremental volume elements, the variances of y and z, and their covariance. The cross product term of the differences of the bias and random errors vanished under the expected value operation. Now, the bias error defined as the sum of its mass-weighted mean and deviation (Johnson and Downey 1975) is given by

$$\delta_{y_i} = \hat{\delta}_y + \delta^*_{y_i}, \tag{10}$$

$$\delta_{z_i} = \hat{\delta}_z + \delta^*_{z_i}, \tag{11}$$

where mean bias errors are given by

$$\hat{\delta}_y = \sum w_i \delta_{y_i}, \tag{12}$$

$$\hat{\delta}_z = \sum w_i \delta_{z_i}. \tag{13}$$

With the expected value of the mass weighted means, $\hat{y}$ and $\hat{z}$, expressed by

$$E(\hat{y}) = \sum w_i E(y_i), \tag{14}$$

$$E(\hat{z}) = \sum w_i E(z_i), \tag{15}$$

the differences of the mean bias error from the difference of the expectation of (2) and (3) is

$$(\delta_y - \delta_z) = E(\hat{y}) - E(\hat{z}). \tag{16}$$

With the combination of (9) through (16), the expected sums of squares becomes

$$E(\mathrm{SS}) = [E(\hat{y}) - E(\hat{z})]^2 + \sum w_i(\delta^*_{y_i} - \delta^*_{z_i})^2 + (\sigma_y^2 + \sigma_z^2) - 2\sigma_{yz}, \tag{17}$$

where for all i the expected value of $\varepsilon^2_{y_i}$ equals σ_y^2, $\varepsilon^2_{z_i}$ equals σ_z^2, and $\varepsilon_{y_i}\varepsilon_{z_i}$ equals σ_{yz}. The bias contribution to the pure error sums of squares is associated with the square of the mean difference of the systematic bias, and the sum of the squares of the differences of deviation bias errors. Note, however, that if the bias errors were identical at each grid point, the first two terms on the right vanish.

In the introduction, three types of numerical errors were discussed: truncation and rounding errors within individual finite difference equations, and then errors from inconsistencies from the differing truncation errors in the definition of derived properties such as θ_e, P_θ (potential vorticity), and other constituents. With relatively few exceptions such as either a numerical inconsistency or an error in transport velocity entering as a bias common to all the time-dependent governing equations, the condition that the bias difference of a derived property $\delta_{yi} - \delta_{zi}$ vanishes from equality of biases should occur infrequently. For equality of biases, the truncation errors of the four individual governing equations that determine the derived property y would need to combine in a very specific way in order to equal the truncation of the trace property z being determined by a single continuity equation. The more desirable and stringent condition to be satisfied is that bias errors vanish at every point or that truncation and rounding errors are minimal and of a random nature, which precludes interaction with the scales being resolved by the model simulation itself. Monitoring of the pure error sums of squares provides relevant information on these matters. The condition in which estimates of the error variance are minimal and remain invariant with time and the resulting relative frequency distribution of errors equilibrates is the ideal one to be satisfied.

Now provided the bias errors and the error covariance σ_{yz} vanish, the relation between the E(SS) and error variances of y and z is given by

$$E(\mathrm{SS}) = \sigma_y^2 + \sigma_z^2. \tag{18}$$

Furthermore, if the variances σ_y^2 and σ_z^2 were homogeneous the unbiased estimate of the variance would be given by

$$\tilde{\sigma} = (\mathrm{SS}/2)^{1/2}, \tag{19}$$

where the overtilde denotes that σ is estimated. If an estimate of variance of one field is known by other means, the sums of squares may be proportioned appropriately.

4. The models

The UW θ–σ gridpoint model (Zapotocny et al. 1994, 1997a) has an average of 19.3 layers and consists of a sigma coordinate PBL 150 mb in vertical extent and an isentropic coordinate-free atmosphere that extends up to 1700 K (~1–2 mb). For this study, the UW θ–σ model uses 2°N–S by 2.5°E–W horizontal resolution. The time differencing, filters, borrowing, etc., in the UW model are described in greater detail in Zapotocny et al. (1997a).

The NCAR CCM Versions 2 (Hack et al. 1993) and 3 (Kiehl et al. 1996) were utilized for this comparison because of their ready access and widespread acceptance for simulating the global climate. In this study, both CCM2 and 3 are run at the standard T42 spectral resolution (approximately 2.8° × 2.8° transform grid) with a vertical resolution of 18 layers. Horizontally the governing equations for mass, vorticity, divergence, and enthalpy are based on an Eulerian spectral transform method with vertical advection being approximated by centered finite differences. Horizontal and vertical transport of water vapor and trace constituent transports are accomplished with shape-preserving SLT (Rasch and Williamson 1990a). The NCAR recommended values of 2.5×10^5 m^2 s^{-1} and 1.0×10^{16} m^4 s^{-1} for ∇^2 and ∇^4 horizontal diffusion coefficients were utilized for divergence, vorticity, and temperature (Hack et al. 1993; Williamson et al. 1995; Acker et al. 1996). The UW model used a 5-min time step while the T42 CCM2 and CCM3 used a 15-min time step. See Hack et al. (1993) and Kiehl et al. (1996) for detailed discussions of CCM2 and CCM3.

5. Numerical simulation of moist reversible processes

The earlier results of Zapotocny et al. (1997b) employing the dry isentropic constraint established that the correlation of θ_e and $t\theta_e$ decreased more rapidly in CCM2 than in the UW θ–σ model and that the scatter was substantially greater. Within the dry isentropic constraint as applied, an appropriate value of θ_e was simply determined from the water vapor, temperature, and pressure. The statistical assessment will now be extended in a detailed analysis of the pure error growth from differences in the simulated θ_e and its proxy $t\theta_e$ for CCM3 and the UW θ–σ model under reversible moist thermodynamics.

The initial global state of 1200 UTC 4 October 1994 for the 10-day simulations was obtained from the strato-

spheric version of the Goddard Earth Observing System 4DDA model (GEOS-1; Schubert et al. 1993), commonly referred to as STRATAN. The proxy $t\theta_e$ for all grid points at the initial time was simply equated to θ_e at corresponding points on the information surfaces of each model, being determined from the temperature, pressure, and specific humidity following Bolton (1980). This direct specification avoided interpolation errors between coordinate systems. All simulations were run moist adiabatically except for the effects of skin friction in all models and the CCM diffusion described above. Under the moist adiabatic constraint of the experiments, the parameterizations involved with radiative transfer, cumulus convection, PBL processes, and so on were suppressed.

In these experiments, continuity equations for water vapor and for cloud water/ice are included explicitly in the governing equations, and heating/cooling from phase changes enters fully in all the governing equations. Three initial experiments comparing results from the UW θ–σ model and CCM3 are carried out in which water vapor condenses and creates cloud water/ice in all simulations. However, in the first experiment evaporation and precipitation does not occur, in the second experiment evaporation of cloud water to vapor occurs without precipitation, and in the third experiment evaporation and precipitation occur. The second experiment is fully reversible in that moist entropy and the global integral of moist static and kinetic energies are conserved, while the third is pseudoreversible in the sense that the internal energy of the falling precipitation is not considered and thus constitutes, however small, an irreversible component (Dutton 1976). As noted, diabatic heating/cooling from phase changes has been appropriately included as a physical process in the thermodynamics of both models, and in the proxy continuity equation, thus there is work of expansion and compression and diabatic vertical transport of all properties in all models.

As a follow-on analysis to study different numerical methods and to illustrate the applicability of the statistical methods, three additional fully reversible experiments are presented in which cloud water condenses and evaporates but without precipitation. The first is a mixed experiment in which CCM3 determines θ_e by its usual simulation from a combination of θ by Eulerian spectral numerics and q by semi-Lagrangian numerics to be compared with CCM2's simulation of $t\theta_e$ by Eulerian spectral numerics. This provides a contrast with the initial set of experiments that employed semi-Lagrangian numerics to simulate $t\theta_e$. The second experiment employs CCM2's Eulerian spectral numerics for all quantities, θ_e from θ and q in comparison with $t\theta_e$. The third experiment utilizes the mass and momentum distributions from a standard 10-day CCM3 simulation, which are then used to simulate the distributions of θ, q_v (water vapor), q_c (cloud water), and $t\theta_e$ by CCM3's semi-Lagrangian numerics over the 10 days and thus determine θ_e from θ and q to compare with $t\theta_e$.

For all experiments in all models, cloud formation with diabatic heating from large-scale condensation occurs with RH $\geq$ 100%. In two of the experiments with reversible transformation of water vapor and cloud water/ice, cloud evaporation with diabatic cooling occurs with RH $<$ 100%. In the experiments where precipitation is included, rain without evaporation occurs with RH $\geq$ 115%. Note that in the absence of evaporation of cloud and precipitation, the converted cloud water is simply accumulated as a trace constituent.

Figure 1 shows the paired relationship of θ_e and $t\theta_e$ for all points at day 10 for the three experiments from the UW θ–σ model (Figs. 1a, 1c, and 1e) and CCM3 (Figs. 1b, 1d, and 1f). Table 1 presents the results for the initial comparison at days 5 and 10. Mean square (MS) differences (equivalent with the total sums of squares in this study) as determined from (1) are listed in the first column. The second column presents root mean squares (rms) differences divided by $\sqrt{2}$ as estimates of the standard deviation of θ_e [See (19)]. The third and fourth columns list the global estimates of θ_e and $t\theta_e$. The difference of the last two columns represents the mean systematic bias $\delta_y - \delta_z$, which equates with $\theta_e - t\theta_e$ [See (16)]. The abscissa in Figs. 1a, 1c, and 1e represents θ_e simulated by the combination of mass, water vapor, and cloud water/ice continuity equations of the UW θ–σ model. The ordinate represents $t\theta_e$ simulated by the corresponding source-free continuity equation. The abscissa in Figs. 1b, 1d, and 1f represents CCM3's simulation of θ_e by the combination of a mass continuity equation, the enthalpy form of the first law simulated by Eulerian spectral numerics, and water vapor and cloud water/ice simulated by semi-Lagrangian transport. The ordinate represents $t\theta_e$ simulated by semi-Lagrangian transport.

The true state, initially and for all future time, is represented by the continuous equiangular line with η equal to ζ everywhere in all the panels. Also, initially by specification y_i equals z_i and ε_{y_i} and ε_{z_i} equal zero at the information points of the model. The differencing of y_i and z_i cancels the corresponding true state values of η_i and ζ_i in (6).

The most striking feature of the paired distributions of θ_e and $t\theta_e$ for the six experiments in Fig. 1 is the minimal scatter in the UW θ–σ results and the relative large scatter and systematic displacement of points from the equiangular line in the CCM3 results. Another striking feature is the similarity of the results among the three experiments for each model. In the case of CCM3, rms differences for the fully reversible simulation in Table 1 range from $\pm$7.70 K at day 5 to $\pm$10.80 K at day 10. The CCM3 rms differences are exceedingly large relative to the UW θ–σ results even though the scatter may appear reasonable on a compressed scale covering 300 K. The minimal scatter from the UW θ–σ model just noted for the panels in Fig. 1 and the small

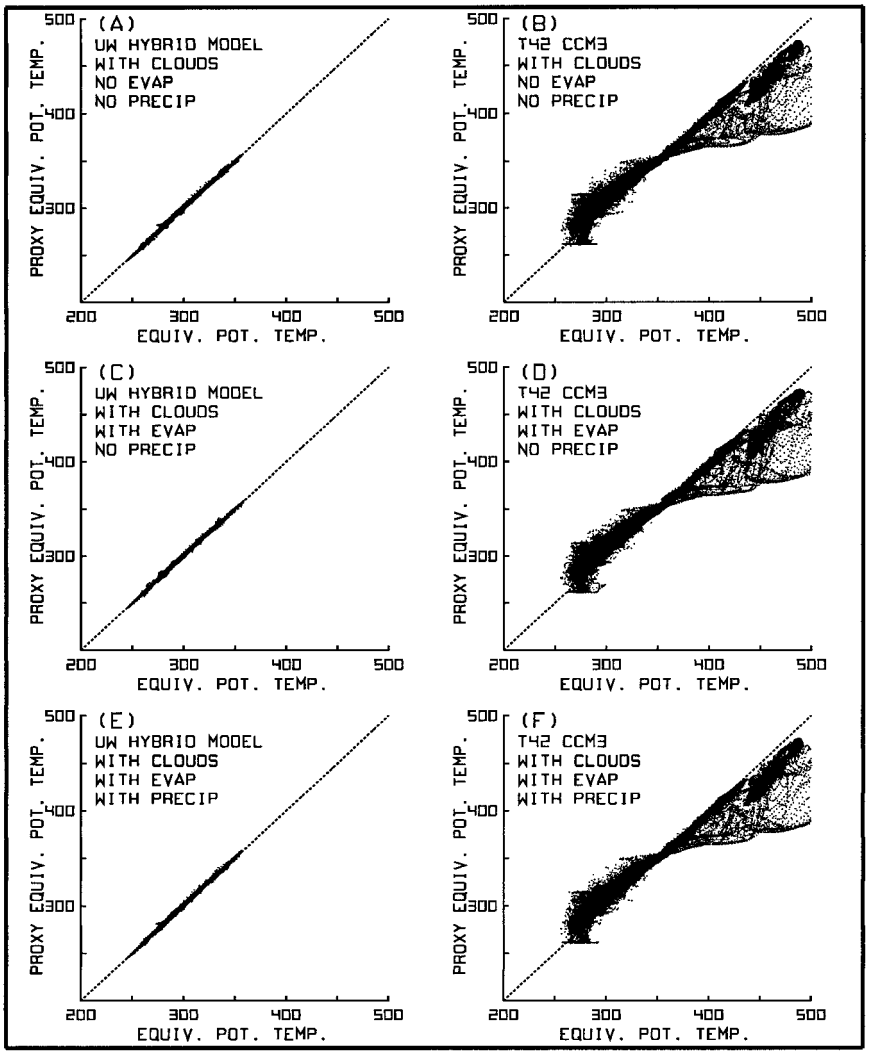

FIG. 1. Bivariate distributions of equivalent potential temperature θ_e (K) and corresponding proxy $t\theta_e$ (K) simulated by the UW θ–σ model and CCM3 for day 10 from three separate global simulations involving phase changes and latent heating/cooling; (a) and (b) cloud condensation without evaporation and precipitation, (c) and (d) cloud condensation/evaporation without precipitation, and (e) and (f) cloud condensation/evaporation and precipitation.

TABLE 1. Mean sums of squares of numerical differences between equivalent potential temperature θ_e and its proxy $t\theta_e$, estimates of rms errors for θ_e (K), and global mean temperatures $\hat{\theta}_e$ (K) and $t\hat{\theta}_e$ (K) for days 5 and 10 determined from three simulations of reversible isentropic processes by UW θ–σ model and by CCM3. The three estimates from each model correspond respectively to Figs. 1a and 1b in which water vapor condenses and clouds form without evaporation; Figs. 1c and 1d in which water vapor condenses, and clouds form and evaporate; and Figs. 1e and 1f in which water vapor condenses, clouds form and evaporate, and precipitation occurs.

		Day 5				Day 10			
		MS	rms	$\hat{\theta}_e$	$t\hat{\theta}_e$	MS	rms	$\hat{\theta}_e$	$t\hat{\theta}_e$
UWθ–σ	CNEP[a]	0.99	0.71	355.2	355.5	0.82	0.64	355.6	355.8
	CENP[b]	1.05	0.73	355.1	355.5	0.85	0.65	355.6	355.9
	CEAP[c]	1.08	0.74	355.1	355.4	0.90	0.69	355.5	355.8
CCM3	CNEP[a]	112.4	7.50	348.9	348.8	220.6	10.50	349.0	348.8
	CENP[b]	118.7	7.70	348.9	348.8	233.2	10.80	349.0	348.8
	CEAP[c]	114.2	7.56	348.9	348.8	224.8	10.60	349.0	348.8

[a] With cloud formation but no evaporation of cloud and no precipitation.
[b] With cloud formation and evaporation of cloud but no precipitation.
[c] With cloud formation, evaporation of cloud, and precipitation.

rms values of ± 0.73 K at day 5 and ± 0.65 K at day 10 for the fully reversible simulation in Table 1 attests to its remarkable capability to simulate moist reversible processes in the presence of diabatic heating (Johnson et al. 1993). In these simulations, the diabatic heating is both a source of internal energy and dry entropy, and a physical process that induces vertical transport of all properties through isentropic surfaces.

In this initial comparison, all the rms calculations determined from the paired differences potentially include bias and random components. If estimates of σ_{θ_e} were to be unbiased, the difference of bias errors would need to vanish, the variance of θ_e and its proxy $t\theta_e$ would need to be equal and the numerical errors would need to be random and independent.

For the atmosphere as a whole, the bias difference $\theta_e - t\theta_e$ in Table 1 that develops by day 10 is 0.2 K for all CCM3 simulations. The bias differences for the UW θ–σ model for the three respective experiments are -0.2 -0.3, and -0.3 K at day 10. Although tabular statistics are not included, the corresponding bias differences at day 10 for CCM2 were 2.5, 2.6, and 2.5 K. These differences for the atmosphere as a whole for CCM3 and the UW θ–σ models are minimal. Interestingly, inspection of the scatter in Fig. 1 suggests that biases layer by layer from the UW θ–σ model vanish, but not for CCM3. The systematic displacement to the left for lower values of θ_e and the right for higher values indicate that bias numerical errors exist in CCM3's simulation of θ_e and/or $t\theta_e$ layer by layer. Later results for the CCM3 differences of θ_e and $t\theta_e$ by layer will reveal an internal cancellation with systematic negative values in the lower troposphere and positive values in the stratosphere that are consistent with the noted systematic scatter in Fig. 1 and also the minimal global mean bias.

The daily tabular values of the percent of water vapor carried as cloud water presented in Table 2 for the two models compare favorably. The initial values of globally averaged precipitable water of 23.13 mm in CCM3 and 23.16 mm in the UW θ–σ model compare favorably with Roads et al. (1992) global value of 23.67 mm from the National Centers for Environmental Prediction operational global assimilated data for December–January–February 1986–89. The UW θ–σ model carries approximately 10% more cloud water than the CCM3 for corresponding experiments at day 10 (see Table 2).

Within the three different experiments for each model the close similarity of the scatter in Fig. 1 stems from the conditions that the water vapor q_v and cloud water q_c transport enjoy an internal consistency. As cloud water q_c is created by condensation, this amount is subtracted from q_v at each grid point. Thus the sum of q_v and q_c corresponds consistently with an implicit total water content q as long as precipitation does not occur. In the UW θ–σ model, the interpolation to determine the amount transported through any surface enters linearly for both q_v and q_c while the intensity of the mass transport $\rho J_\theta u$, $\rho J_\theta v$, and $\rho J_\theta \dot{\theta}$ through the appropriate surfaces at any given time step is identical in all of the time-dependent governing equations. The flux form of the governing equations in the UW θ–σ model ensures global conservation with respect to transport. A fixer that borrows locally to remove negative values satisfies conservation of water substances locally.

TABLE 2. Daily values of the percent of day-0 total water vapor carried as cloud water for the three UW θ–σ and three CCM3 global simulations identified in Fig. 1.

Case/day	With clouds, no evap or precip	With clouds and evap, no precip	With clouds, evap and precip
UW θ–σ			
0	0.00	0.00	0.00
1	1.64	1.27	0.57
2	3.71	2.82	0.61
3	5.85	4.05	0.59
4	7.66	4.85	0.55
5	9.02	5.44	0.55
6	10.06	5.69	0.52
7	11.05	5.95	0.48
8	11.81	5.87	0.44
9	12.54	6.46	0.40
10	13.21	6.95	0.36
CCM3			
0	0.00	0.00	0.00
1	2.55	1.85	0.49
2	4.63	3.21	0.51
3	6.39	4.03	0.52
4	8.01	4.42	0.50
5	9.10	4.67	0.44
6	10.00	4.71	0.36
7	10.72	4.71	0.32
8	11.30	4.81	0.32
9	11.87	4.96	0.31
10	12.35	5.02	0.28

For the CCM and its semi-Lagrangian transport, both of the fields q_v and q_c are interpolated from model grid points to departure points by the same cubic spline function and both are transported from the departure point to a common model grid point by the same trajectory displacement. Thus, there is little source of error as consistency between the distribution of q_v and q_c is maintained even as thermodynamic phase changes occur. This of course provides no insight into how well the semi-Lagrangian simulation of water substances conserves the water substances during the 10 days since semi-Lagrangian methods do not ensure global conservation with respect to transport. Nonconservation enters locally from the use of cubic functions to interpolate the water vapor, and also cloud water/ice from the Gaussian grid to the departure points. A fixer ensures constancy of water vapor globally by requiring that the global integrals of water vapor before and after application of semi-Lagrangian transport are equal at each time step. The combination of the methods of interpolation and global fixer permit internal mixing of moist static energies.

Figure 2 shows the day-10 spatial distribution of differences, θ_e minus $t\theta_e$, for the top sigma surface of the

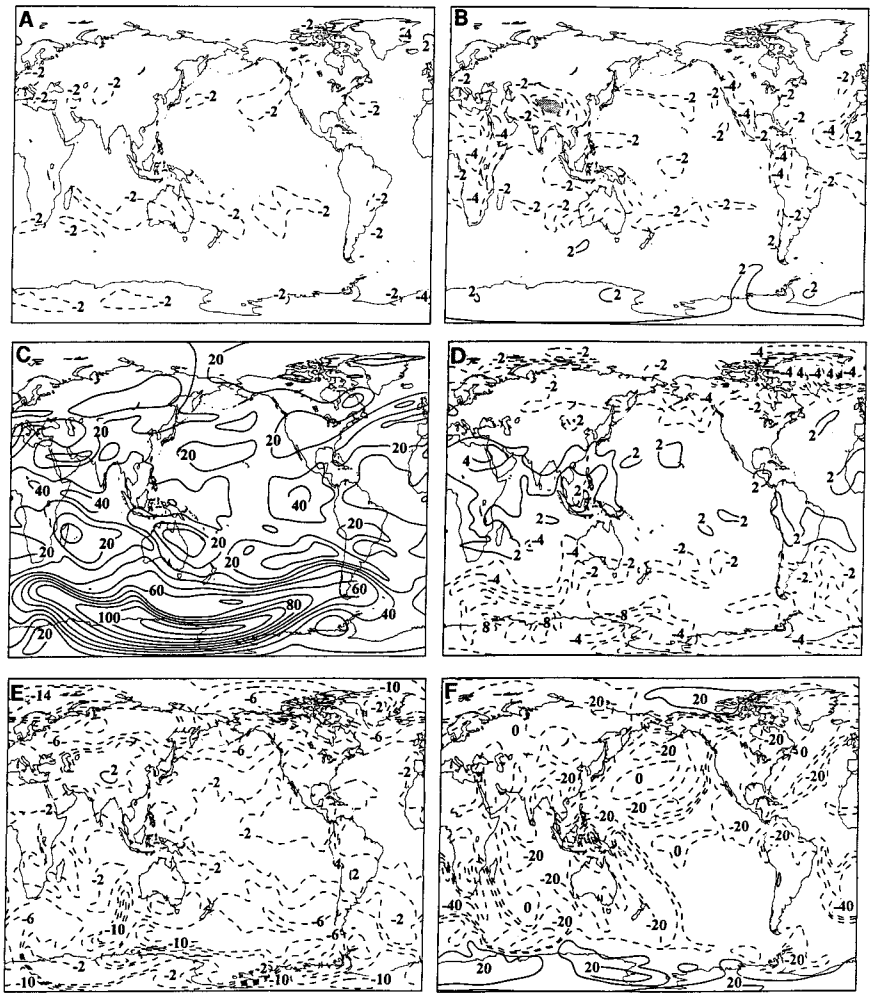

FIG. 2. Simulated day-10 difference fields of θ_e (K) minus $t\theta_e$ (K) for the (a) top sigma surface of the PBL and (b) 308-K surface from the UW θ–σ model, and for the (c) 64H, (d) 251H, (e) 598H, and (f) 992H surfaces from the T42 CCM3. The shaded area near the Himalaya in (b) indicates where the 308-K surface is underground. The contour interval is 2 K in (a), (b), (d), and (e) and 10 K in (c) and (f).

PBL (Fig. 2a), the 308-K surface (Fig. 2b) from the UW θ–σ model, and the 64H (Fig. 2c), 251H (Fig. 2d), 598H (Fig. 2e), and 992H (Fig. 2f) surfaces from CCM3. The H for each surface in the CCM2/3 identifies the hybrid sigma-isobaric vertical coordinate system that transitions from pure sigma at the earth's surface to isobaric coordinates in the upper atmosphere. The UW θ–σ surfaces were chosen to both bracket and intersect the interface between θ–σ domains, and as such, the results estimate error associated with transport processes through the interface. Low- and midtropospheric layers, and a stratospheric layer are shown for CCM to illustrate the relatively poor results in the lower troposphere and stratosphere and relatively consistent results near the level of nondivergence.

The UW θ–σ differences are generally less than 2 K in both layers with exceptions exceeding 4 K at a few isolated locations. The day-10 values on the top sigma layer (Fig. 2a) range from -4 K over Antarctica and eastern Greenland to 2 K northeast of Iceland. The 308 K (Fig. 2b) differences range from -4 K near regions of elevated orography to slightly greater than 2 K over Antarctica. In contrast, the 992H CCM3 day-10 differences (Fig. 2f) are generally negative and range from -30 K over numerous areas to 20 K along the coastline of Antarctica. The differences at the 598H level (Fig. 2e) of the midtroposphere are also generally negative reaching values of -10 K along the coast of Antarctica, but the magnitudes are significantly smaller than in the lower-tropospheric layers. With more frequent occurrence and also the largest errors occurring in extratropical latitudes, this geographical distribution of errors clearly indicates that the nonconservation stems from the difficulties in accurately simulating transport of moisture and also other trace constituents within the vertically sheared flow of baroclinic waves in extra-

tropical latitudes. Inspection of the differences reveals a systematic zonally varying structure of differences that extends vertically over at least four of the lowest layers (not shown) in extratropical and polar latitudes. This systematic vertical-zonal structure indicates the impact of the vertical motion within baroclinic waves and the development of truncation errors from vertical advection within the sheared flow of the westerlies.

Excessively large positive bias departures exceed 110 K on the 64H surface in the stratosphere over Antarctica (Fig. 2c). Since the errors at this level are all positive and display coherent patterns, clearly the need for a statistical model that includes degrees of freedom for both a mean bias and a spatial bias deviation sums of squares as provided by (17) is evident.

Overall, the results in Figs. 1 and 2 at day 10 clearly illustrate that differences of the paired values of θ_e and $t\theta_e$ remain small under the moist reversible experiments in the UW θ–σ model even near the interface between θ and σ model domains. The error differences in the low and even in the midtroposphere for CCM3 are large while the differences in the stratosphere are exceedingly large. The runaway differences in the lower stratosphere (Fig. 2c) stem from a serious numerical inconsistency between CCM3's semi-Lagrangian and Eulerian spectral methods in the simulation of the dry entropy component of θ_e, which will be discussed in more detail later.

The early Community Climate Models CCM0B and CCM1 employed Eulerian spectral numerics throughout the model in contrast with CCM2/3, which employ semi-Lagrangian numerics for trace constituents but Eulerian spectral numerics otherwise. In their efforts to develop and employ semi-Lagrangian numerics in CCM2/3, Williamson and Rasch (1989) and Rasch and Williamson (1990a,b) focused on the elimination of several shortcomings in simulating water vapor transport from Eulerian spectral numerics (e.g., spectral ringing and rain, Gibbs phenomena, negative water vapor, etc.). They clearly demonstrated improvements in a series of two-dimensional numerical experiments. In a follow-on study comparing CCM1 and CCM2, Rasch and Williamson (1991, 1990b) show that large changes in model climate were obtained by replacing Eulerian spectral with semi-Lagrangian numerics for the water vapor equation.

As identified by Rasch and Williamson (1990b) there is an inconsistency between computing trace constituent vertical advection by semi-Lagrangian transport and temperature vertical advection by finite difference methods. The differences in the lowest layers, however, cannot be attributed solely to vertical advection since the vertical motion vanishes at the lower boundary. Here differences are magnified in the lowest layers of the troposphere by the Gibbs phenomena (Navarra et al. 1994) and spectral ringing. Visual inspection of CCM3's θ_e field in lower layers simulated without the horizontal diffusion described above provides supporting evidence of further degradation (not shown). Zapotocny et al. (1997b) showed that although the scatter about the equiangular line from an experiment employing a version of CCM2 using corresponding Eulerian spectral numerics for water vapor and trace constituent transport was large, there were no apparent systematic biases. See Fig. 2f from Zapotocny et al. (1997b). The fields of water vapor transport in the lowest layers from simulations employing CCM2/3 semi-Lagrangian transport are decidedly more coherent than the fields simulated by Eulerian spectral methods (not shown). Still there are systematic bias and random errors from the differences between θ_e and $t\theta_e$ in CCM3 as shown for the 992H surface in Fig. 2f that range between -30 and 20K. While the differences obtained in this study were not unexpected, the surprise is the magnitude of both the random and bias components that develop in a matter of days from CCM3's numerical inconsistencies.

6. Detailed assessment of numerical inaccuracies for CCM3

The different numerical formulations in CCM2/3 and the flexibilities attained in utilizing Eulerian spectral numerics horizontally, finite differences vertically, and semi-Lagrangian numerics for constituents proved to be ideal for illustrating the merit of the statistical applications set forth to assess the internal consistency and accuracy in the simulation of conservation of derived properties. The lack of consistency in the CCM3 simulations of θ_e and $t\theta_e$ is clearly evident in Figs. 1 and 2 from the substantial bias and random errors that develop by day 10. The findings (not shown) from like simulations by CCM2 are almost identical. Box et al. (1978) emphasizes that a detailed inspection of error fields and statistics is all important for isolating inconsistencies in the development of a model and for gaining insight into the means to improve models. The results will now focus on differing reasons for the errors in the low troposphere and stratosphere and also their latitudinal and temporal dependency. In particular, the temporal and spatial nature of the errors will be examined in more detail for the fully reversible processes presented in Fig. 1d and Table 3, and relative frequency distributions of the differences will be compared.

Bivariate distributions representing days 2.5, 5, 7.5, and 10 are presented in Figs. 3a, 3b, 3c, and 3d, respectively, while the corresponding distributions for six levels 992, 970, 598, 251, 991, and 64H at day 10 are offered in Fig. 4. Recall CCM3's asymmetric scatter distributions for day 10 in Figs. 1b, 1d, and 1f portraying systematic departures to the left of the equiangular line in the lowest layers and to the right in the stratospheric layers. If there were no systematic differences in numerics involving the simulation of θ_e from enthalpy by Eulerian spectral and water substances by semi-Lagrangian methods versus $t\theta_e$ by semi-Lagrangian numerics, the scatter of the paired variables in the bivariate distributions would be symmetric about the equiangular

TABLE 3. Rms error statistics for θ_e (K) from a reversible CCM3 simulation of equivalent potential temperature θ_e and its proxy $t\theta_e$ for the layers indicated, and for the whole atmosphere at days 2.5, 5, 7.5, and 10. Also included are the global average equivalent potential temperature $\hat{\theta}_e$ and its proxy $t\hat{\theta}_e$ for day 10 and the percentage of total atmospheric mass in each layer.

	rms				$\hat{\theta}_e$		$t\hat{\theta}_e$	
Layer/day	2.5	5	7.5	10	0	10	10	% mass
5H	14.3	13.3	13.6	13.7	1123.1	1124.3	1124.8	0.5
13H	8.0	8.0	8.3	7.7	782.5	782.7	785.2	1.4
33H	24.5	37.8	46.5	52.2	577.7	577.4	506.3	2.8
64H	9.5	15.8	20.7	24.1	460.0	459.4	430.1	3.5
99H	3.0	4.6	6.4	8.1	400.4	400.3	394.0	3.5
139H	1.5	2.0	2.5	3.4	370.6	371.0	368.3	4.5
189H	1.1	1.4	1.7	1.9	350.2	351.1	349.8	5.6
251H	0.9	1.1	1.3	1.5	336.5	338.1	338.1	6.8
325H	0.8	0.9	1.0	1.0	328.3	330.6	331.1	7.9
409H	0.8	1.0	1.1	1.2	323.2	325.8	326.8	8.9
501H	1.1	1.5	1.8	2.0	319.1	321.5	323.8	9.6
598H	1.6	2.2	2.6	3.0	315.6	318.3	321.9	9.8
695H	2.0	2.9	3.5	4.0	313.8	316.0	320.9	9.5
786H	2.6	3.6	4.5	5.1	312.4	314.0	320.3	8.7
866H	3.2	4.6	5.6	6.3	312.1	311.2	319.3	7.2
929H	3.5	5.2	6.4	7.3	315.8	307.5	317.0	5.3
970H	4.0	6.2	7.5	8.5	317.9	302.2	312.6	2.9
992H	4.4	7.7	9.9	10.8	318.0	297.9	308.4	1.5
Global	5.1	7.7	9.6	10.8	348.8	349.0	348.8	100.0

line at each level and also more or less uniform along the line.

Table 3 presents estimates of the rms differences of θ_e for all levels in CCM3 for days 2.5, 5, 7.5, and 10 [see (19)]. The rms differences vary vertically and increase temporally at all levels except between 7.5 and 10 days for 13 and 325H. The growth of differences is largest in the initial 2.5-day time interval. After five days, the rate of increase is reduced. The rms difference statistics in the lowest layer increase from zero to ± 4.4 K in 2.5 days and to ± 10.8 K in 10 days. The minimum occurs at the 325H level where the rms is ± 0.8 K at

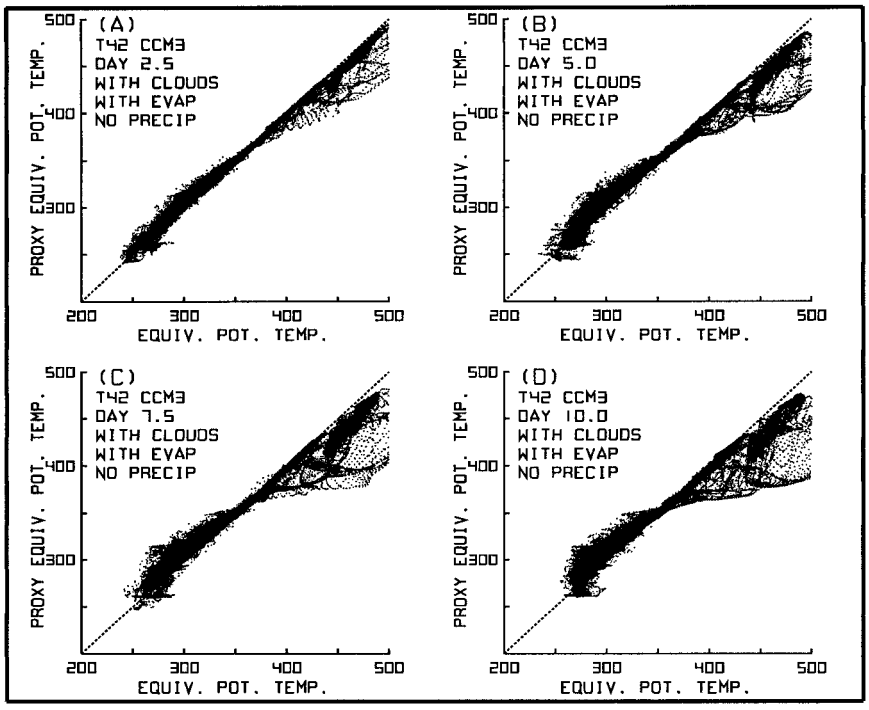

FIG. 3. Bivariate distribution of equivalent potential temperature θ_e (K) simulated by CCM3 versus its proxy $t\theta_e$ (K) simulated by semi-Lagrangian transport for the following times: (a) day 2.5, (b) day 5, (c) day 7.5, and (d) day 10.

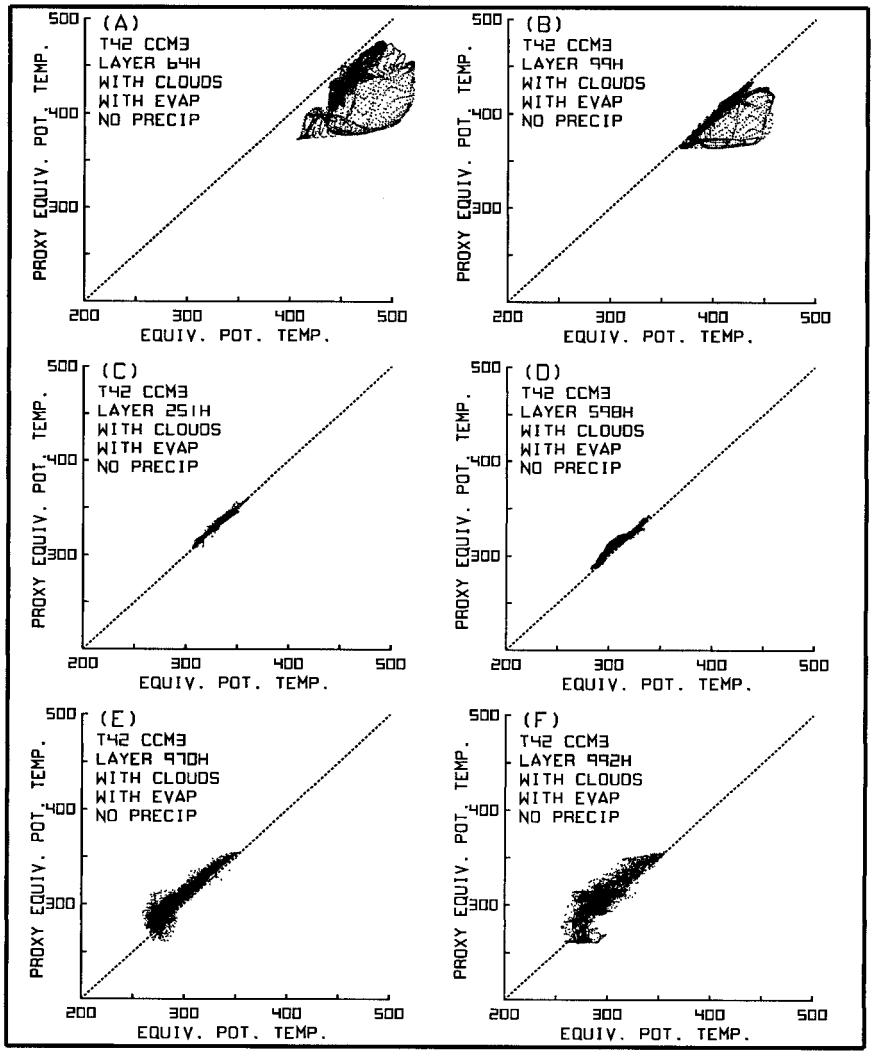

FIG. 4. Bivariate distribution of equivalent potential temperature θ_e (K) at day 10 simulated by CCM3 versus its proxy $t\theta_e$ (K) simulated by semi-Lagrangian transport for the following levels: (a) 64H, (b) 99H, (c) 251H, (d) 598H, (e) 970H, and (f) 992H.

day 2.5 and ± 1.0 K at day 10. In the third and fourth layers from the top, the differences are extremely large at day 10 with the rms being ± 52.2 and ± 24.1 K in the 33 and 64H layers, respectively. An integration utilizing a time step of 7.5 min verified that the results from the 15-min time step are robust and that the large differences are not due to computational instability.

Although the first inclination is to dismiss these differences as reasonable because of different numerical algorithms, such action cannot be substantiated. The differences are simply too large and systematic. Recognition must be made of the condition that both numerical methods estimate an evolving state of a system responding to Lagrangian sources of properties and thus differences are a measure of the uncertainties of climate models with regard to numerics. Clearly the rms calculations reveal that the variances for θ_e and $t\theta_e$ are not homogeneous and the numerical errors are not independent and random. The spatial and mean differences between θ_e and $t\theta_e$ in the stratosphere are incomprehensively large from physical considerations and cannot be supported with respect to transport nor from dry and moist adiabatic processes. In the stratosphere, the lack of vertical resolution to simulate θ_e in concert with certain numerical inconsistencies in the vertical advection between the Eulerian spectral simulation of θ and the semi-Lagrangian simulation of $t\theta$ involving cubic splines combine to create the largest error. The strategy set forth here portraying tabular values and field distributions all with respect to time and the follow-on experiments presented in the next section will serve to isolate these difficulties.

Now the discussion will focus on results for the six representative levels portrayed in Fig. 4 and the relation

of the bivariate distributions and biases level by level. The upper and lower two levels (Figs. 4a, 4b, 4e, and 4f) are characterized by relatively large scatter about the equiangular line, while the mid-tropospheric layers in Figs. 4c and 4d have much less scatter. The bias components given by the difference of θ_e and $t\theta_e$ as estimates of $E(\theta_e)$ minus $E(t\theta_e)$ at day 10 from Table 3 are +29.3 K at 64H, +6.3 K at 99H, +0 K at 251H, −3.6 K at 598H, −10.4 K at 970H, and −10.5 K at 992H. In the low stratosphere θ_e decreases from day 0 to 10 by 0.6 K at 64H and 0.1 K at the 99H, while in the low troposphere θ_e decreases 20.1, 15.7, and 8.3 K at the 992, 970, and 929H layers, respectively. In contrast $t\theta_e$ decreases from day 0 to 10 by 29.9 K at 64H and 6.4 K at 99H in the stratosphere. In the troposphere it decreases 9.6 and 5.3 K at 992 and at 970H respectively, while it increases 6.3 K at 598H. The most consistent CCM3 results in the sense of minimum random and bias differences occur within the mid-to upper troposphere. Since, for the global atmosphere θ_e increases 0.2 K while $t\theta_e$ remains the same, there are compensating biases among the layers for both θ_e and $t\theta_e$, such that the global mean changes are minimal. Still these systematic compensating changes that differ markedly in the vertical between the simulations by Eulerian spectral and semi-Lagrangian numerics over the 10 days imply markedly different vertical exchange of both dry and moist static energies as well as differences in entropy exchange. With suppression of physical parameterizations, the vertical exchange must occur through explicit transport or advection.

The bias and random differences in CCM3's lowest three layers, being large from considerations of sensible and latent energy balance, also pose unusual difficulties in the simulation of moist adiabatic processes in that the saturation-specific humidity doubles for every 10 degrees increase in temperature. Furthermore, if normally distributed the rms statistic implies that approximately one-third of the random differences are larger than ±one sigma. The spatial patterns of bias differences in Figs. 2c–f reveal a latitudinal dependence discussed earlier with the largest differences occurring in extratropical latitudes. Large differences from vertical truncation errors develop in baroclinic regions where wind shear and temperature gradients are maximized. These differences also potentially pose difficulties between numerics and any parameterization that serves to exchange entropy vertically since the latter is nearly always dependent on vertical stability criteria. The differences in the vertical distribution of area mean temperatures also imply that the model's radiative flux of energy will differ substantially.

Now, note in Table 3 that the temporal changes in CCM3 stratospheric simulations of θ_e determined from enthalpy by Eulerian spectral numerics and q by semi-Lagrangian numerics between days 0 to 10 are minimal, while the corresponding temporal 10-day changes for $t\theta_e$ by semi-Lagrangian numerics show decreases of 71.4 K at the 33H level, and 29.9 K at the 64H level. The conclusion is that CCM2/3's semi-Lagrangian numerics to determine $t\theta_e$ are flawed, at least at these two levels. Such large temporal changes cannot be supported in view of the essentially dry adiabatic conditions imposed by the lack of water substances in the stratosphere. In this case the two different numerical methods lead to markedly different temporal changes.

The culprit for the extremely large bias and random differences in the stratosphere, including the tropopause region and to some extent lesser bias and random errors in the lowest layers of CCM3 rests with the use of Hermite cubic interpolants. Hack et al.'s (1993) and Kiehl et al.'s (1996) descriptions based on the earlier extensive numerical work of Rasch and Williamson (1990a,b) are now summarized within the context of why the biases and also the rms errors in the stratosphere are exceedingly large in the stratosphere and also relatively large in the lower layers.

Within semi-Lagrangian numerics, the location of the departure point above or below a given surface is determined by the sense of the vertical motion while the vertical displacement of the trajectory from the departure to the arrival point is dependent on the intensity of the vertical motion and the time step. In regions of upward vertical motion, the departure points for all levels are located below the surface of arrival points. In regions of downward vertical motion, the departure points for all levels are located above the surface of arrival points. The Hermite cubic interpolant provides for a continuous specification of the property throughout the vertical extent of the model domain. However, as implemented the continuity of the first and second derivatives is limited to each interval of interpolation extending from η_k to η_{k+1}, that is, the two levels bounding the departure point. As such, the variation expressed by the first, second, and third derivatives that specifies the vertical profile of the property throughout the model domain is discontinuous at the information levels $k = 1, 2, 3, \ldots, K$. See Fig. 1 of Kiehl et al. (1996) for vertical structure of CCM3 and numbering of information levels.

As part of the vertical component of the SLT scheme, the determination of the Hermite cubic interpolant that specifies the distribution of a trace constituent within each interval of interpolation requires property values at the two levels η_2 and η_3 bounding the departure point, say q_2 and q_3, and also corresponding estimates of Hermite derivatives, say d_2 and d_3. See (3.c.20) and (3.c.21) of Kiehl et al. (1996).

For the purpose of illustrating the lack of continuity, assume that the departure property q_d lies between levels η_2 and η_3 and with downward vertical motion is carried to level η_3. The estimate of the departure point property q_d is determined as a weighted combination of the properties, q_2 and q_3, and the Hermite derivatives, d_2 and d_3, all respectively located at η_2 and η_3. In turn, the Hermite derivative estimates are determined as a

weighted combination of four data, q_1, q_2, q_3, and q_4, from the four adjacent levels, the two nearest levels located above the point of departure, η_1 and η_2, and the two below, η_3 and η_4. Now assume that a corresponding departure point lies within the lower adjacent interval of interpolation bounded by η_3 and η_4 and is carried upward from the departure point to the same arrival level η_3. In this case, however, the cubic derivatives d_3 and d_4 are determined from property values q_2, q_3, q_4, and q_5 and the departure value is determined from q_3, q_4, d_3, and d_4. Since the derivatives d_2 and d_3 for the downward displacement are determined from q_1, q_2, q_3, and q_4, while the derivatives d_3 and d_4 for the upward displacement are determined from q_2, q_3, q_4, and q_5, the Hermite cubic derivatives at the common arrival level η_3 are not unique. Note that d_3 with downward displacement does not equal d_3 with upward displacement. As such, the vertical profile of q as determined by the successive Hermite cubic interpolants in CCM3 layer by layer is only piecewise continuous.

The analytic implications of bias from piecewise continuity are evident from uniqueness property of polynomials in that any polynomial of degree less than or equal to n that passes through n discrete points is unique (Greenspan 1971). Now note that the functional form of the expression for the departure point [(3.c.17), Kiehl et al. 1996] within the interval of interpolation bounded by η_2 and η_3 readily expands into a unique polynomial in powers of η in the form of

$$q_d = A_o + A_1\eta + A_2\eta^2 + A_3\eta^3.$$

Here, apart from conditions to satisfy monotonicity, the set of coefficients A_o, A_1, A_2, and A_3 determined for downward vertical motion, $w < 0$, are individually and uniquely related to the four property values q_1, q_2, q_3, and q_4, while for upward vertical motion, $w > 0$, a corresponding but different set is determined from the property values q_2, q_3, q_4, and q_5. As such, the Hermite interpolants used for CCM3 only provide for piecewise polynomial interpolation with $\partial q/\partial\eta$ and $\partial^2 q/\partial\eta^2$ being discontinuous at the arrival levels $k = 1, 2, 3, \ldots, K$ (e.g., p. 142, Atkinson 1978).

Given the discontinuous nature of derivatives at the arrival surfaces and the noncentered nature of the arrival surface and also the departure point relative to the four points of information, aliasing readily results between even and odd terms within a polynomial determination of the departure point property q_d, particularly in regions when the variation of the property is large. As such, bias errors readily develop within the increments of change $(q_d - q_3)$ with $(w < 0)$ and corresponding change $(q_d - q_3)$ with $(w > 0)$. The net effect of the piecewise polynomial representation of the rapid increase of θ_e in the stratosphere in conjunction with semi-Lagrangian transport in CCM3 is to induce extremely large biases in the upper layers. These sources of error are compounded whenever the vertical resolution varies substantially as it does in the upper levels. The lack of continuity for first- and higher-order derivatives at the arrival level in conjunction with rounding errors also enhances the random error component.

Now consider the combination of piecewise polynomial representation and semi-Lagrangian transport in the simulation of reversibility for both dry and moist thermodynamic processes. With the first- and higher-order derivatives discontinuous at the arrival surfaces, the process of vertical advection $\dot{\eta}\partial q/\partial\eta$ fails to be accurately replicated by the semi-Lagrangian numerics. Note that at the arrival surface $\partial q/\partial\eta$ is double valued being dependent on whether the motion is upward or downward. This condition compromises the reversibility, a point noted more generally by Egger (1999).

A further complication encountered in semi-Lagrangian numerics is the specification of boundary conditions. With the absence of information exterior to the domain for layers nearest the upper and lower boundary, there is no means to estimate the first- and higher-order derivatives on the upper or lower boundary directly from the model simulation of transport processes. Thus the dependent property in this case θ_e is assumed constant from the boundary surface to the first interior model level. Then the Hermite derivative d_1 for the interval of interpolation from η_1 to η_2 is assumed zero, while the derivative d_2 for the same interval is equated to the derivative d_2 for the adjacent interval η_2 to η_3. As such, the Hermite cubic interpolant remains continuous from η_3 to η_1. Inspection of θ_e and $t\theta_e$ at day 10 in Table 3 reveals that the conditions imposed that ensure continuity at the first, second, and third derivatives in the uppermost two layers preclude any substantive mean bias from developing at the levels η_1 and η_2. Still, the nature of the enlongated elliptic scatter for the level η_2 (not shown) being orientated at an angle relative to the equiangular line indicated that systematic bias differed spatially with upward and downward displacement. This lack of systematic bias (see Table 3) for these two layers also bears indirect evidence of the need to insure continuity of derivatives across the arrival surface.

Now note that extremely large bias and random error develops in the third layer, where with downward vertical motion the interval of interpolation is affected by the boundary condition, while, with upward vertical motion to the same arrival level, the property is free from the constrained boundary conditions. The combination of the constained boundary conditions along with the vertically uncentered cubic approximations in the upper layers and the freedom from constraints in lower layers is the prime reason for the development of the largest bias and rms errors to develop on the arrival level η_3.

The pattern of differences for the arrival level η_3 in Fig. 2c indicates a wavenumber-one distribution in the Southern Hemisphere with the vertical motion in the stratosphere being asymmetric across the South Pole. An asymmetric vertical motion field across the pole in combination with the resulting differences of semi-Lagrangian departure point values, vertical gradients of θ_e,

TABLE 4. Rms error statistics for θ_e (K) from a reversible simulation of θ_e and its proxy $t\theta_e$ in which overlapping quadratic polynomials have been utilized in lieu of the CCM3's Hermite cubic interpolants for the semi-Lagrangian transport of water vapor (q_v), cloud water (q_w), and $t\theta_e$. CCM3 Eulerian spectral numerics were utilized for simulation of mass, momentum, and enthalpy. The results for equivalent potential temperature θ_e as determined from simulated enthalpy and water vapor and its for the $t\theta_e$ are presented for the layers indicated, and for the whole atmosphere at days 2.5, 5, 7.5, and 10. Also included are the global average equivalent potential temperature $\hat{\theta}_e$ and its proxy $t\hat{\theta}_e$ for day 10 and the percentage of total atmospheric mass in each layer. The format of this table is identical with Table 3 to provide for ready comparison.

	rms				$\hat{\theta}_e$		$t\hat{\theta}_e$	
Layer/day	2.5	5	7.5	10	0	10	10	% mass
5H	14.2	12.9	13.3	13.9	1123.1	1124.2	1123.6	0.5
13H	2.7	2.5	2.9	2.8	782.5	782.7	782.4	1.4
33H	2.2	2.3	2.6	2.8	577.7	577.5	575.6	2.8
64H	1.6	1.5	1.7	1.6	460.0	459.5	458.6	3.5
99H	1.0	1.1	1.2	1.2	400.4	400.4	399.5	3.5
139H	0.8	0.9	1.0	1.0	370.6	371.0	370.3	4.5
189H	0.7	0.8	0.9	0.9	350.2	350.9	350.6	5.6
251H	0.7	0.8	0.7	0.8	336.5	337.7	337.8	6.8
325H	0.5	0.6	0.6	0.6	328.3	329.8	329.9	7.9
409H	0.5	0.6	0.7	0.7	323.2	325.0	324.9	8.9
501H	0.5	0.6	0.8	0.7	319.1	321.1	320.8	9.6
598H	0.7	0.8	0.9	0.9	315.6	317.9	317.5	9.8
695H	0.7	0.9	0.9	0.9	313.8	315.9	315.6	9.5
786H	1.1	1.1	1.1	1.1	312.4	313.6	313.6	8.7
866H	1.2	1.4	1.5	1.6	312.1	310.9	310.6	7.2
929H	1.2	1.8	2.0	2.2	315.8	309.0	310.2	5.3
970H	2.2	3.4	3.9	4.3	317.9	305.8	307.4	2.9
992H	4.8	6.3	7.7	8.4	318.0	301.7	307.4	1.5
Global	1.6	1.7	1.9	2.0	348.8	348.9	348.8	100.0

and variation in layer depth readily accounts for the systematic bias. In summary, the conditions for the development of bias errors are particularly fertile in the stratosphere where the vertical gradients of θ are extreme, the vertical gradients change markedly, and large-scale quasi-stationary planetary waves persist.

Unequivocal evidence for the conclusion that the source of the difficulty in CCM3 stems from the piecewise Hermite interpolants is now offered from the results of a test integration. In this test integration using CCM3 semi-Lagrangian numerics, the Hermite cubic interpolants were replaced by overlapping second-order Lagrangian polynomials in the vertical in combination with linear distance weighting to yield a resultant third-order polynomial (Greenspan 1971; Whittaker and Petersen 1977; Reames and Zapotocny 1999). Table 4 presents results from the replacement with overlapping quadratic interpolants corresponding with the results in Table 3. A comparison reveals that the rms errors of the upper troposphere and lower stratosphere are markedly reduced in conjunction with a reduction for all levels and all times. The two exceptions of small increases of 0.4 K at 992H for day 2.5 and 0.2 K at 5H for day 10 are inconsequential relative to the marked reductions attained nearly everywhere. Interesting enough the rms differences for the upper- and lowermost levels for the four times in Tables 3 and 4 are similar. This similarity is due to the use of CCM3's boundary conditions of constancy in the upper- and lowermost layers for the overlapping quadratic functions.

Even more startling from comparison of θ_e and $t\theta_e$ at day 10 is the reduction of nearly all biases to a few tenths of degrees. The runaway bias in the stratosphere has been completely suppressed. The largest bias of 5.7 K developed in the lowest layer, while one to two degree biases occurred in four other layers.

This strategy of weighted overlapping quadratic polynomials plus upper and lower boundary conditions just noted yields a unique continuous unconstrained vertical representation of $t\theta_e$ and its first derivative throughout the entire model domain (Reames and Zapotocny 1999). Thus the vertical displacement from the departure to the arrival point at a given level whether positive or negative as the proxy for advection $\dot{\eta}\partial q/\partial\eta$ remains well represented and provides for reversibility. While other numerical methods may be preferable in terms of degree of continuity, monotonicity, and/or convexity (Rasch and Williamson 1990a), the immediate problem here has been to identify the source of the bias difference in the lower troposphere and stratosphere. The minimal bias and greatly reduced rms provides unequivocal evidence that the Hermite cubic interpolants used in CCM3 were not an optimum choice.

In an extensive study comparing climate states simulated by semi-Lagrangian numerics versus CCM2 Eulerian spectral numerics (Williamson and Olson 1994) and also CCM3 (Williamson et al. 1998), the issue of why climate model simulations utilizing semi-Lagrangian numerics and the respective physical parameterizations of each model developed a colder extratropical and tropical tropopause was addressed. Despite their argument that semi-Lagrangian numerics are formally

more accurate, Williamson and Olson (1994) noted in their concluding statement of comparison with CCM2 Eulerian spectral numerics that somehow ''the smaller computational error results in a worse climate.'' They also argue that the CCM2 physical parameterizations have been tuned to offset the conjectured error from lower-order accuracy of CCM2 numerics. They then suggest that the semi-Lagrangian model must be retuned to achieve an optimal state.

In the later study, Williamson et al. (1998) were only able to obtain convergence of results regarding mean tropopause temperatures for the Held–Suarez test case (Held and Suarez 1994) between CCM3 and their all semi-Lagrangian model by substantially increasing vertical resolution, first doubling and then quadrupling. The CCM3 simulated tropospheric and stratospheric temperatures remained virtually independent of changes in resolution in the three comparison tests while the semi-Lagrangian simulated temperatures evolved with changes of resolution and only converged to the CCM3 profiles with the highest resolution. At the uppermost layer, a systematic bias always remained between CCM3 and the all semi-Lagrangian model, which was displaced upward as the semi-Lagrangian model increased its resolution. Williamson et al. (1998) attributed this bias to the different ''advection top boundary conditions'' between CCM3 and the semi-Lagrangian model, a conclusion in agreement with the findings from the use of overlapping weighted quadratic interpolants just discussed.

In a response to suggestions that models based on semi-Lagrangian numerics are more accurate (e.g., Pellerin et al. 1995; Lin and Rood 1996), Leslie and Dietachmeyer (1997) state from their comparison of Eulerian and semi-Lagrangian methods that unless appropriate orders of schemes are considered, the conclusion by others ''that semi-Lagrangian schemes are superior in accuracy, and produce less noise than Eulerian schemes'' should be discounted. They established that when semi-Lagrangian and Eulerian schemes of the same order are applied to the test case of ''warm bubble'' convection, there are almost indiscernible differences between the simulations.

While it is somewhat inappropriate to apply strictly Leslie and Dietachmeyer's conclusions to this study of reversibility in weather and climate models since the physical basis carried out in these experiments differs greatly, the circumstantial evidence of the unbiased simulations for CCM3 with semi-Lagrangian numerics determined by a linear combination of quadratic interpolants provides an interesting perspective concerning numerics. In their comparison of climate simulations between CCM2 and their semi-Lagrangian model utilizing Hermite cubic interpolants and constrained boundary conditions, Williamson and Olson's (1994) quandary is why utilization of semi-Lagrangian numerics with ''smaller computational error results in a worse climate.'' In actuality, the piecewise Hermite cubic interpolants utilized in a discrete model with varying grid resolution and strong vertical variation of temperature through the tropopause region in proximity to the upper boundary will readily yield estimates of derivatives at the top and bottom of the layer for departure point interpolation, which are biased by the combination of temperature structure and boundary conditions. Consequently, assessments of relative numerical accuracies based on one- and two-dimensional advection tests may be misleading. Furthermore, claims that a certain order of accuracy for semi-Lagrangian numerics with unequal spatial resolution in the presence of bias and random components of numerical error are not necessarily well founded particularly with the lack of continuity for first derivatives at the arrival levels. The degree of aliasing from higher-order three-dimensional variation is a function of spacing between the departure points, the grid points structure of arrival points, the degree of disconinuity, and the displacement of the departure point relative to the centroid of points utilized in determining the polynomial interpolant. Furthermore, within a statistical perspective of bias and random numerical errors superimposed on a continuum, the expected uncertainty of the departure point in terms of its second moment of the random error component varies spatially within the layer of interpolation.

7. Detailed assessment for the UW θ–σ model

Table 5 details UW θ–σ rms statistics for θ_e from the fully reversible moist isentropic experiment in which clouds form and evaporate but do not precipitate. The magnitudes of the day-10 bias from the UW θ–σ model given by the difference of θ_e and $t\theta_e$ in Table 5 are equal to or less than 0.1 K everywhere above 316 K. These maximum bias errors involving both potential temperature and water substances in the UW θ–σ model are one or more orders of magnitude less than the maximum bias differences in CCM3. Likewise, the rms statistics for θ_e from the UW θ–σ model are strikingly small relative to the rms statistics from CCM3.

Within the layers extending from 332 to 370 K, which do not intersect the sigma domain of the UW θ–σ model, the rms errors range from ± 0.1 K to ± 0.2 K at day 10. In higher layers, where water vapor is minimal, specific humidity being on the order of 10^{-5}, the zero values for rms means that by virtue of rounding actual values are less than ± 0.05 K. Within isentropic layers that intersect the sigma domain, rms values range from ± 0.5 K to ± 1.5 K at day 10.

Empirical frequency distributions of the CCM3 and UW θ–σ differences of θ_e and $t\theta_e$ for the same four time periods as for the bivariate distributions in Fig. 3 are presented in Fig. 5. The class interval in Figs. 5a and 5b for CCM3 is 1 K, while the class interval in Figs. 5c and 5d for the UW θ–σ model is 0.1 K. The vertical axes in Figs. 5a and 5c are scaled linearly, while the vertical axes in Figs. 5b and 5d are scaled logarith-

TABLE 5. Rms error statistics for θ_e (K) determined from a reversible UW θ–σ model simulation of equivalent potential temperature θ_e and its proxy $t\theta_e$ for the layers indicated, and for the whole atmosphere for days 5 and 10. Also included are the global average equivalent potential temperature $\hat{\theta}_e$ (K) and its proxy $t\hat{\theta}_e$ (K) for days 0 and 10 and the percentage of total atmospheric mass in each layer.

	rms		$\hat{\theta}_e$	$\hat{\theta}_e$	$t\hat{\theta}_e$		
Layer/day	5	10	0	10	10	% mass	$\bar{p}\theta$
1250 K	0.0	0.0	1250.0	1250.0	1250.0	1.1	6
700 K	0.0	0.0	700.0	700.0	700.0	1.7	20
555 K	0.0	0.0	555.0	555.0	555.0	1.9	38
485 K	0.0	0.0	485.1	485.1	485.1	1.8	56
445 K	0.0	0.0	445.1	445.1	445.1	1.4	73
415 K	0.0	0.0	415.1	415.1	415.1	2.1	92
390 K	0.0	0.0	390.1	390.1	390.1	2.3	114
370 K	0.1	0.0	370.1	370.1	370.1	3.4	141
356 K	0.1	0.1	356.2	356.1	356.1	2.7	167
348 K	0.2	0.2	348.6	348.5	348.5	4.7	196
340 K	0.3	0.2	341.5	341.6	341.5	6.7	238
332 K	0.2	0.2	334.6	334.8	334.8	8.5	296
324 K	0.4	0.5	329.4	329.9	329.8	10.8	371
316 K	0.8	0.7	325.4	325.6	325.7	12.5	471
308 K	1.4	1.2	321.2	321.1	321.9	12.9	588
300 K	1.4	1.4	317.1	317.4	318.4	10.7	708
292 K	1.5	1.5	303.2	303.7	304.9	7.3	805
284 K	1.4	1.3	290.6	291.6	292.7	4.7	876
276 K	1.2	1.1	281.6	281.5	282.0	2.1	926
268 K	0.9	0.9	270.8	271.6	271.8	0.7	952
260 K	1.0	0.9	262.3	261.9	262.0	0.1	960
252 K	0.3	0.6	253.5	253.0	252.9	0.0	961
Global	1.1	1.0	354.4	354.3	354.6	100.0	

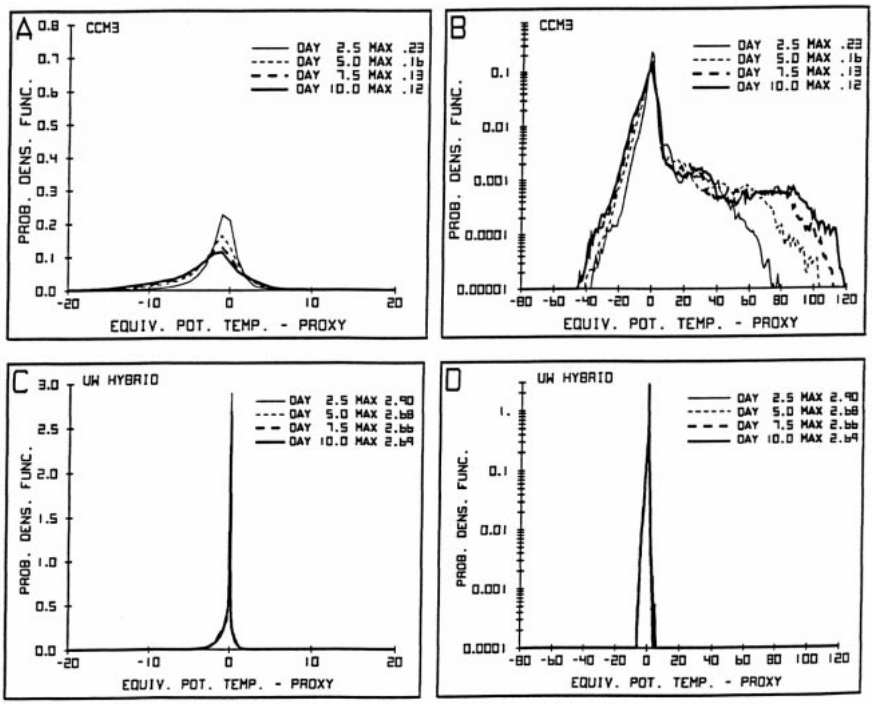

FIG. 5. Empirical relative frequency distributions of simulated differences of equivalent potential temperature θ_e (K) and its proxy $t\theta_e$ (K) for days 2.5, 5, 7.5, and 10. Plots (a) and (b) portray results from CCM3 and (c) and (d) portray those from the UW θ–σ model. Vertical axes on the left are scaled linearly, while the vertical axes on the right are scaled logarithmically to retain larger outliers.

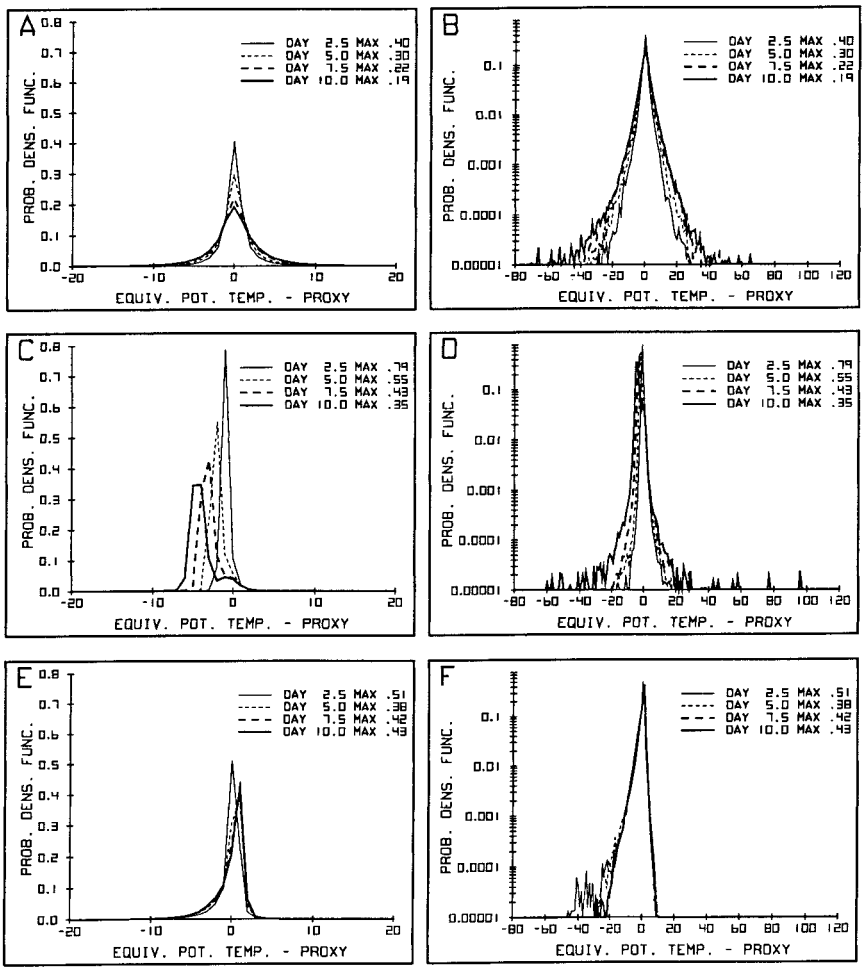

FIG. 6. Empirical relative frequency distributions of simulated differences of equivalent potential temperature θ_e (K) and $t\theta_e$ (K) for days 2.5, 5, 7.5, and 10 for three follow-on experiments: (a) and (b) are for the mixed CCM3/2 experiment, (c) and (d) are for the CCM2 all-Eulerian spectral experiment, and (e) and (f) are for the CCM3 all–semi-Lagrangian experiment. Vertical axes on the left are scaled linearly while vertical axes on the right are scaled logarithmically to retain large outliers.

mically to retain the large outliers. All logarithmic scales extend over five decades, from 10^{-5} to 1 for CCM2/3 and from 10^{-4} to 10 for the UW θ–σ model. Since for each time step, there are approximately 1.5×10^5 differences entered for each frequency distribution, a logarithmic scaling of the vertical axis over five decades from 10^{-5} to 1 is required to retain the largest outliers.

With linear scaling of the vertical axis and a 1 K class interval, the ordinate values represent the percentage of the differences within the given class interval and the sum of ordinate value for each class interval times the class interval is unity. With logarithmic scaling, the area within the frequency distribution does not integrate to unity. All of the ordinate values of the relative frequency distributions for CCM2/3 are less than unity. See Figs. 5a, 5b, and Fig. 6. With the 0.1 K degree class intervals for the UW θ–σ model, the ordinate values exceed unity. See Figs. 5c and 5d. In this case the sum of the product of 0.1 K class interval and the ordinate values as shown sum to unity. Although not shown due to lack of resolution needed to reveal the high degree of accuracy, the ordinate values for the UW θ–σ model with a class interval of 1 K are 0.63, 0.60, 0.62, and 0.64 for the four time periods. For example, the day-10 values for the UW θ–σ model just stated indicate that 64% of the differences lie within ± 0.5 K of the maxima of the frequency distribution while for CCM3 only $\pm 12\%$ lie within the same interval.

Inspection of the two frequency distributions for CCM3 in Figs. 5a and 5b reveals a steady increase of the spread with time and thus a steady decrease in the frequency of differences contained within the interval of the maximum occurrence. The maximum of 0.23 at day 2.5 in CCM3 decreases to 0.12 at day 10, a decrease corresponding with 11 parts in 23. Inspection of the bivariate distributions identifies this increasing system-

atic spread in the frequency distribution in Figs. 5a and 5b with the temporal increase of asymmetries about the equiangular line for the temperatures ranging from 250 to 325 K and above 375 K in Fig. 3. The scatter by level for the same range of temperatures is evident in Fig. 4. These temperature differences developed from the boundary constraints on $t\theta_e$ from the semi-Lagrangian numerics and correspond with the levels of large bias and random differences identified earlier by the spatial analysis within the low troposphere and the stratosphere.

In Fig. 5a, the maximum frequency of occurrence shifts toward the left with time. The distribution also shifts toward the left with time. Thus there is a time dependency of the CCM3 bias and frequency distribution of differences. This shift of the maximum is not evident in Fig. 5b although it is associated with the temporal increase of the frequency of negative differences on the order of -20 K in the region extending vertically from 0.000 01 to 0.1. At the same time, in the region extending vertically from 0.000 01 to 0.001 there are very large positive differences that increase with time from 80 to 120 K. While the magnitude of this increase of differences is larger, their number is smaller. This temporal increase of the large differences indicates that the numerical errors are of sufficient magnitude to interact with the true field. With a total of 1.5×10^5 differences globally, the number of very large θ_e differences is on the order of 150 points. In attempting to locate sources of model errors, these are the points to which attention is needed.

Inspection of the corresponding spread and maximum frequency of occurrence for the UW θ–σ model in Figs. 5c and 5d reveals minimal changes. The maxima for the UW θ–σ model within a class interval of 0.1 K are 2.90, 2.68, 2.66, and 2.69 at days 2.5, 5.0, 7.5, and 10, respectively. Although in this case, the decrease from day 2.5 to day 10 is approximately 2 parts in 30, the increase in the maximum frequency of occurrence within the 0.1 class interval from day 7.5 to day 10 is evidence of an equilibration of the distribution of differences. This equilibration indicates that the ideal of noninteraction of the error field with the true state has been attained.

8. Follow-on experiments

In modeling transport of properties and Lagrangian sources, all numerics aim to replicate the Euler relation, either directly or indirectly. Without knowledge of the true atmospheric state involved, there is no a priori means to determine which numerical methods are more accurate in the simulation of reversibility and conservation of entropy apart from the comparison set forth herein. The contrast of large differences from the comparison of the rms statistics and the bias differences between CCM3 and the UW θ–σ model is symptomatic of the uncertainties of numerics in the simulation of reversibility in weather and climate models.

For reasons just noted and to demonstrate the merit of assessing reversibility via the strategy employed, the results from three follow-on experiments are presented in the form of frequency distributions and abbreviated tables. The first follow-on experiment termed mixed employs CCM3 Eulerian spectral and semi-Lagrangian numerics to simulate θ and q respectively in determining θ_e and CCM2 Eulerian spectral numerics to simulate $t\theta_e$. The results from utilizing Eulerian spectral numerics to simulate $t\theta_e$ contrast with the earlier results in which CCM3 semi-Lagrangian numerics simulated $t\theta_e$. Although some minor changes were made in the CCM3's Eulerian spectral numerics from CCM2's, the resulting differences in numerics are small relative to the differences between Eulerian spectral and semi-Lagrangian numerics. The results from the second follow-on experiment employing CCM2 to simulate θ_e as function of θ and q and also $t\theta_e$, all by Eulerian spectral numerics, contrasts with those from the third follow-on experiment employing CCM3 to simulate θ_e as a function of θ and q and also $t\theta_e$, all by semi-Lagrangian numerics. Since the capability to simulate a trace constituent by Eulerian spectral methods was not carried forward from CCM2 to CCM3, CCM2 was employed to carry out the mixed experiment and the all-Eulerian spectral experiment.

As a sequel in the development of NCAR's climate models, Williamson et al. (1998) have developed a semi-Lagrangian version of CCM3 and noted differences in the simulation of climate states. The all–semi-Lagrangian results here are not determined using Williamson et al.'s (1998) all–semi-Lagrangian version of CCM3, but are based on CCM3's standard configuration utilizing governing equations still expressed in Eulerian spectral form to simulate the mass, momentum, and enthalpy structure throughout the 10-day integration. Then utilizing the mass and momentum from this integration in conjunction with the initial state structure of θ, q, and $t\theta_e$, CCM3's semi-Lagrangian numerics were utilized to simulate the state structure of θ, q and $t\theta_e$ throughout the 10 days with θ_e being calculated from θ and q in the determination of the sums of squares. This strategy employing semi-Lagrangian numerics is consistent with that utilized in chemical transport models.

Table 6 presents an abbreviated set of statistics for these three follow-on experiments providing rms statistics at days 5 and 10 and the systematic difference ($\theta_e - t\theta_e$) at day 10 by level and globally. The results for the first experiment utilizing CCM3 to determine θ_e and CCM2's Eulerian spectral representation of $t\theta_e$ reveal that the large systematic and spatially varying stratospheric differences that were evident in the initial CCM3 experiments have been eliminated. Within the 33 and 64H levels, the rms differences at day 10 are now ± 2.5 and ± 2.1 K respectively, while the bias differences are 0.1 and -0.1 K. A comparison for the same levels of the initial values for θ_e from Table 3 and $t\theta_e$ at day 10 from the mixed CCM2/3 experiment in Table 6 reveals

TABLE 6. Rms error statistics for θ_e (K) from three follow-on experiments determined from reversible model simulations of equivalent potential temperature θ_e and its proxy $t\theta_e$ for the layers indicated, and for the whole atmosphere at days 5 and 10. Also included are the bias ($\hat{\theta}_e - t\hat{\theta}_e$) (K) and $\hat{\theta}_e$ (K) at day 10 and the percentage of total atmospheric mass in each layer. In the mixed experiment, CCM3 determines θ_e from a combination of θ by Eulerian spectral numerics and q by semi-Lagrangian numerics in comparison with CCM2 Eulerian spectral simulation of $t\theta_e$. In the second follow-on experiment CCM2 simulates θ and q to determine θ_e, and $t\theta_e$, all by Eulerian spectral numerics. In the third follow-on experiment CCM3 simulates θ and q to determine θ_e and $t\theta_e$, all by semi-Lagrangian numerics for trace constituents.

	Mixed CCM2/3				CCM2 all Eulerian spectral				CCM3 all SLT				
	rms		$\hat{\delta}$	$\hat{\theta}_e$	rms		$\hat{\delta}$	$\hat{\theta}_e$	rms		$\hat{\delta}$	$\hat{\theta}_e$	
Layer/day	5	10	10	10	5	10	10	10	5	10	10	10	% mass
5H	4.5	6.5	1.4	1124.3	2.1	2.8	1.3	1124.2	0.2	0.2	0.2	1125.0	0.5
13H	3.0	3.4	0.6	782.7	1.2	1.4	0.6	782.7	0.7	0.9	1.3	786.5	1.4
33H	2.0	2.5	0.1	577.4	0.7	0.7	0.2	577.5	0.5	0.7	0.9	507.3	2.8
64H	1.6	2.1	−0.1	459.4	0.5	0.5	0.0	459.5	0.4	0.5	0.6	430.7	3.5
99H	1.3	2.1	0.1	400.3	0.4	0.8	−1.1	399.1	0.4	0.6	0.8	394.8	3.5
139H	0.9	1.7	0.2	371.0	0.9	1.8	−2.5	368.3	0.4	0.6	0.8	369.1	4.5
189H	0.8	1.5	0.2	351.1	1.1	2.3	−3.2	347.6	0.6	0.7	0.7	350.5	5.6
251H	0.7	1.3	0.2	338.1	1.3	2.7	−3.8	334.1	1.4	1.0	0.4	338.5	6.8
325H	0.7	1.3	0.3	330.6	1.5	2.9	−4.1	326.2	1.6	1.2	0.2	331.3	7.9
409H	0.9	1.5	0.3	325.8	1.5	3.1	−4.3	321.2	1.4	1.3	0.1	326.9	8.9
501H	1.1	1.7	0.0	321.5	1.6	3.2	−4.5	317.1	1.6	1.4	0.0	323.8	9.6
598H	1.4	1.9	0.0	318.3	1.6	3.2	−4.6	313.7	1.5	1.3	−0.2	321.7	9.8
695H	1.9	2.4	−0.1	316.0	1.7	3.3	−4.7	311.4	1.5	1.4	−0.5	320.4	9.5
786H	2.3	3.0	0.2	314.0	1.7	3.4	−4.7	309.2	1.4	1.5	−0.8	319.5	8.7
866H	3.0	3.8	0.6	311.2	1.7	3.5	−4.7	305.9	1.7	1.8	−1.2	318.1	7.2
929H	3.1	5.6	−0.3	307.5	1.8	4.6	−4.8	302.9	2.0	2.1	−1.4	315.6	5.3
970H	3.9	9.9	0.0	302.2	2.0	9.1	−5.0	297.2	2.3	2.6	−1.8	310.8	2.9
992H	6.3	18.3	1.8	297.9	2.9	15.0	−4.7	291.4	2.7	3.9	−2.9	305.5	1.5
Global	2.0	3.7	0.2	349.0	1.5	3.8	−3.8	343.8	1.4	1.4	−0.2	348.7	100.0

that the changes in θ_e over the 10-day period are 0.0 and -0.6 K, respectively.

In this situation where the extremely large differences simulated by CCM3 occur in the stratosphere, the source of the difficulties actually resides with the dry component of $t\theta_e$ in the CCM2/3. Eulerian spectral and semi-Lagrangian numerics simulate distinctly different trajectories as both attempt to simulate reversibility. Since the stratosphere is essentially devoid of water substances, the model simulations of θ_e and $t\theta_e$ essentially reduce to simulations of θ and $t\theta$ as the flow evolves essentially through dry adiabatic conditions. As such, the large biases that develop in the stratosphere for $t\theta_e$ do not directly impact CCM3 Eulerian spectral simulations of enthalpy in the uppermost layers.

Although to a large extent this absolves the standard CCM3 from the suggestion that its simulated stratospheric temperatures by the governing equations have extremely large bias, it does not relieve it from the issue that the temperature structure being determined by Eulerian spectral numerics is not appropriate to the structure of cloud water/ice, chemical species, hygroscopic aerosols, and other trace constituents, all of which are or would be determined by semi-Lagrangian numerics. By virtue of the adiabatic nature of the large-scale exchange of entropy, the implicit temperature structure that corresponds with the semi-Lagrangian transport of constituents is inconsistent with temperature structure simulated by the CCM3's Eulerian spectral numerics. Furthermore, the biases that develop in the lowest layers between θ_e and $t\theta_e$ impact climate simulations and accuracies in simulating reversibility. Very simply the CCM3 semi-Lagrangian numerics detailing the water vapor transport are inconsistent with the Eulerian spectral numerics detailing the dry entropy transport.

An overall comparison of the rms errors for the three follow-on experiments at day 10 in Table 6 reveals that nearly all are less than in the initial CCM3 results except for the lowest two layers. Here the rms differences for the 970 and 992H layers from the mixed CCM2/3 are ± 3.9 and ± 6.3 K at day 5 increasing to ± 9.9 and ± 18.3 K at day 10. The CCM2 all-Eulerian spectral numerics rms differences are ± 2.0 and ± 2.9 K at day 5 increasing to ± 9.1 and ± 15.0 K at day 10. Both are unusually large and unacceptable. The corresponding rms differences of ± 2.6 and ± 3.9 K at day 10 for the same layers in the CCM3 all–semi-Lagrangian simulation reveals a marked improvement relative to either CCM2 or CCM3 in their standard configuration. Compare rms values and biases in Table 3 and Table 6. The standard CCM3 and all-Eulerian spectral CCM2 biases in the lowest layer of -10.5 and -4.7 K, respectively, have been reduced to -2.9 K in the CCM3 all–semi-Lagrangian simulation. Except for the four lowest layers, all other bias differences within the CCM3 all–semi-Lagrangian simulation are reduced to approximately ± 1 K or less. The overall results clearly indicates that CCM3 all–semi-Lagrangian numerics lead to a marked reduction of rms and bias differences. There is also some indication of an equilibration of the rms differences for the CCM3 all–semi-Lagrangian experiment, except for possibly the lowest layers. At the same time, rms and bias difference of ± 2.6 and -1.8 K, and ± 3.9 and -2.9 K, respectively in the 970 and 992H layers are not insignificant. In particular, the magnitude of the bias in nearly all levels of the CCM3 all–semi-Lagrangian simulates exceeds that in the mixed CCM2/3 experiment.

The extreme changes for θ_e over the 10 days with decreases in temperature of 70.4 and 29.3 K in the 33 and 64 H stratospheric levels from the all–semi-Lagrangian numerics still remain. Compare the simulated layer means θ_e for the 33 and 64 H levels at day 10 from the CCM3 all–semi-Lagrangian simulation in Table 6 with the corresponding θ_e for days 0 and 10 and $t\theta_e$ for day 10 from the standard CCM3 simulation in Table 3. These temperatures at day 10 as discussed earlier are unrealistic since such large changes in θ_e from day 0 and 10 cannot be supported from physical considerations. One must also recognize that the near elimination of the large CCM3 bias between θ_e and $t\theta_e$ at the 33 K and 64 H levels in the CCM3 all–semi-Lagrangian simulation has not removed the source of difficulties involving the constrained boundary conditions and lack of continuity for the first- and higher-order variation at the model information levels. In this case, both θ and θ_e as trace transport constituents have common biases that upon subtraction eliminate the biased difference.

The frequency distributions for these three follow-on experiments are presented in Figs. 6a–f in which the class interval is one degree. In contrasting the results for the follow-on experiments with the earlier results in Figs. 5a and 5b, first note that the spread as a measure of the random error is much greater in the standard CCM3 stimulation; thus, indicating that its random error inaccuracies in stimulating conservation of θ_e are the greatest. The maximum of the frequency distribution for the standard CCM3 experiment that decreases from 0.23 at day 2.5 to 0.12 at day 10 in Fig. 5 contrasts in Fig. 6 with maxima of 0.40, 0.79, and 0.51 for the three additional experiments at day 2.5, respectively, and 0.19, 0.35, and 0.43 at day 10. As such, the decrease of the maxima of the frequency distribution reveals a spreading of the distributions with time thus indicating random error growth in all simulations.

In contrasting the maxima of the frequency distributions for the CCM2 all-Eulerian spectral versus the CCM3 all–semi-Lagrangian numerics, note that the relative maxima of 0.79 for CCM2 at day 2.5 exceeds that of CCM3 semi-Lagrangian maxima of 0.51, thus indicating a lesser random error component for Eulerian spectral numerics in the initial 2.5-day period. However, by day 10 CCM3's value of 0.43 exceeds CCM2's value of 0.35. This indicates greater rate of increase of the random error component by a more rapid diffusion/dispersion of enthalpy and water substances when simu-

lated by all-Eulerian spectral methods than with the basic or semi-Lagrangian numerical versions of CCM3. The rapid decrease in accuracy particularly during the last five days is indicated by the rms values of ± 1.2 K at day 2.5, ± 2.9 K at day 5, ± 7.2 K at day 7.5, and ± 15.0 K at day 10 from inspection of the spatial distribution. Table 6 presents values at days 5 and 10 while values for 2.5 and 7.5 days are simply transcribed from output statistics. The doubling of the rms difference every 2½ days is evidence of exponential growth of the random error component. Inspection of the spatial distribution at the four times reveals that the origin of the instability stems largely from Gibbs phenomena and spectral ringing. By day 10, bias differences ranging from -5 to -3 K have developed at all levels below 189H. A corresponding rapid decrease in accuracy with nearly exponential error growth is present in the lowest layer of the mixed CCM2/3 simulation that also stems from Gibbs phenomena. However, in this case, there was minimal if any systematic development of a bias component from the condition that two different models were utilized in the comparison. The small spikes in Figs. 6b and 6d detail extremely large outliers that result from spectral ringing in both the mixed and CCM2 all-Eulerian spectral simulations.

Inspection of Fig. 6c for the all-Eulerian spectral numerics also provides convincing evidence for the development of a time-dependent bias component as the maxima of the frequency distribution systematically shifts with time toward negative values and develops a bimodal structure. Inference indicates that bias errors have reached sufficient magnitude to interact with the true field, while the shift indicates that the interaction of the field bias δ^* with the true state and the bimodal structure are likely situation dependent.

There is also some shift of the maxima of the relative frequency distribution in the standard CCM3 and all–semi-Lagrangian simulations (see Figs. 5a and 6f). The tabular statistics discussed earlier revealed a marked time-dependent bias difference that developed in CCM3's 33 and 64H layers from the semi-Lagrangian numerics. With respect to the accuracies as determined by the 2.5-day rms differences, on a percentage scale from day 2.5 to day 10 the maxima of the relative frequency distributions for the mixed experiment decreases by 28%, the all-Eulerian spectral experiment by 56%, and the all–semi-Lagrangian experiment by 16% where the class interval is 1 K. The percentage decreases for the UW θ–σ model was 7% for a class interval of 0.1. Within a class interval of 1 K, the maxima of the relative frequency increased from 0.63 to 0.64, which corresponds with a 1.4% increase. These differences in percentage decreases combined with the differences in class interval, the range of differences needed to capture the largest outliers, and the persistent occurrence of large outliers in all CCM experiments reveal that the ideal result of a nearly time-independent relative distribution of numerical errors free of bias and minimal rms as achieved for the UW θ–σ model has not been achieved by any of the CCM simulations.

At this point, some caution regarding conclusions based on a limited analysis is in order. Note in the comparison of the frequency distributions in Figs. 5 and 6, the statistics for the ordinate value of the maximum frequencies and the spread over the 10 days certainly suggest that the CCM3 all–semi-Lagrangian simulation is more accurate in conserving θ_e than the standard CCM3 simulation as well as the CCM2 all-Eulerian spectral simulation. Such a conclusion would be without merit, since very large systematic biases including one in excess of 50 K are present in both θ_e and $t\theta_e$ in the upper layers of CCM3 all–semi-Lagrangian simulation. Note this extreme bias that develops with the semi-Lagrangian simulations over the 10 days, however, is not present in θ_e as simulated by the standard CCM3. Here a comparison of tabular results for different numerical algorithms determines that common biases in θ_e and $t\theta_e$ exist, but have been eliminated by subtraction. This is an example of the limitation of utilizing only one numerical model and simply inspecting one aspect of the strategy set forth in this study to assess inaccuracies.

As Box et al. (1978) emphasize, a detailed inspection of the errors in all forms is essential. In essence the only information available to improve the modeling of physical processes within a given model resides with a comprehensive study of the errors of the model's own simulation. Even more information is gained from an assessment of the numerical accuracies of several models.

9. Some implications and further applications

In his theoretical analysis of the underlying reasons for the coldness of simulated climate states, Johnson (1997) emphasized that an attribute of isentropic coordinates is to minimize aphysical sources of entropy from numerics. He noted that an isentropic model will remain free of aphysical sources of dry entropy from mixing by numerical diffusion/dispersion since the vertical flux of mass and entropy is Lagrangian and the horizontal exchange occurs within layers of equal entropy. Since potential temperature is the surrogate for dry entropy, and also an independent coordinate variable, the mass continuity equation in effect determines the entropy distribution. Thus changes in the hydrostatic mass distribution determine changes in temperature and pressure consistently through the Poisson relation without any numerical error as long as the model conserves mass. Furthermore, the flux finite difference form for the coupled set of nonlinear governing equations in the UW θ–σ model explicitly ensures internally within the isentropic domain consistent transport of the mass with all other simulated properties. Since the mass transport uniquely determines dry entropy transport, this also ensures the consistent transport of simulated properties

with entropy transport. The only degree of freedom for errors in θ_e to develop in isentropic models apart from the necessities of borrowing and filtering is through the rounding and truncation errors in the determination of water vapor and cloud water/ice. For these reasons, the uncertainty expressed by the rms differences of θ_e and $t\theta_e$ stems primarily from differences of truncation and rounding errors within the coupled set of equations utilized in the calculation of the transports of water vapor and of cloud water/ice in regions of extreme gradients and the partitioning of the same quantities as grid volumes emerge and submerge through the θ–σ interface of the UW θ–σ model (Pierce et al. 1991). At the same time, the flux form also ensures global conservation of energy, entropy, water vapor, cloud water/ice, and other constituents in concert with global mass conservation. The results in this study that the simulation of moist reversible processes by models utilizing isentropic coordinates have markedly greater accuracy than models utilizing sigma or other coordinate systems reinforces these earlier results (Johnson et al. 1993; Zapotocny et al. 1996, 1997a,b).

Theory supports the claim that the capability to stimulate accurately the entropy structure throughout the atmosphere is of first-order importance. A central thrust of this study is to develop and apply a statistical strategy for assessment of the internal consistency of a set of coupled finite difference equations of mass, energy, and water substances to simulate reversible atmospheric processes and the appropriate conservation of dry and moist entropy in accord with the Navier–Stokes equations for the continuum. With the residence time of atmospheric water vapor being 10 days, a corresponding period of time was selected in this study for integrations focusing on hydrologic processes internal to the atmosphere.

The intrinsic uncertainty of global observational capabilities including limited sampling in time and space and the nonlinearity of the governing equations precludes a direct determination of the biases and random errors that develop in research and operational prediction models. The true atmospheric state is never known exactly. However, from the statistical analysis based on pure error variance, the true state does not need to be known in order to make a first-order assessment of the merit of different numerics and model coordinate representations in simulating reversible processes that are intrinsic to entropy conservation within the fully developed nonlinear structure of weather and climate models. The strategy assesses a model's capability to simulate consistently the future state of a property f and its proxy tf utilizing equality of the initial states by specification and determination of the sum of squared differences as a function of time within which the true state being common to f and tf subtract. The sums of squares function assesses error growth from rounding and truncation errors and resulting inconsistencies within the coupled set of nonlinear governing equations. The strategy developed provides field differences for spatial and temporal assessment and includes a relative frequency distribution, all of which provide insight into the accuracy of a given model. Robust statistical measures are used to assess the accuracy of numerical algorithms directly throughout the entire model domain in relation to the appropriate conservation of moist entropy and related properties and, in the sense that the true state is implicitly represented, revealing, but conservative assessments of bias and random error components from numerics are ascertained. The conservative nature of the assessment stems from the condition that if f and tf have common biases, their biases cancel just as the common true state cancels.

While the method set forth is based on simple classic concepts, the statistical strategy developed here involving assessment of pure error spatially and temporally simplifies direct comparison of statistics among models and thus invites further applications among models. Since the frequency distribution of the error differences with division of the gridpoint mass by total atmospheric mass estimates a probability density distribution, all of the statistics are in effect normalized and may be directly compared among models. This avoids the necessity to interpolate results from different models to a common coordinate system for comparison or validation, thus precluding errors from vertical interpolation. The method is ideally suited to assess numerical accuracies encountered in the simulation of key thermodynamic processes involving reversibility and capabilities to conserve potential temperature, equivalent potential temperature, potential vorticity, and water substances without knowledge of the true state. Furthermore, of all the atmospheric properties, the above are ones that are crucial to accurate simulation of thermodynamic, hydrologic, and chemical processes.

There is the general trust in simulations of the climate state by some that the uncertainty from numerics is minimal. This trust, however, must be reexamined with respect to accuracies in simulating dry and moist entropy and reversible processes. There is also the need to ascertain the impact of positive definite aphysical sources of entropy in limiting the accuracy of atmospheric predictions. Zonally mean temperature biases on the order of 10°C are frequently observed in climate models (Boer et al. 1991, 1992) with larger biases observed regionally. Johnson (1997, 2000) has called attention to positive definite aphysical sources of entropy as a source of bias errors in temperature and that the existence of aphysical sources of entropy from numerical mixing of energy constitutes a fundamental physical and logical basis for the ''coldness of climate models.'' Within the CCM2/3 simulations of this study, much larger spatial differences of θ_e and $t\theta_e$ were embedded within the baroclinic structure of extratropical and polar latitudes and thus aphysical sources of entropy from mixing of latent and sensible energies must be present (Johnson 1997, 2000). A critical difficulty from such a bias is a corresponding error in saturation-specific humidity that doubles for

each 10°C increase in temperature. Thus there is a corresponding inherent strong dependence of hydrologic and chemical processes on such biases.

With judicious modification to the Lagrangian source for the trace continuity equation, the strategy may be extended to study the accuracy of a model in simulating reversibility as different dry and moist convective parameterization algorithms are introduced and tested in model development. The strategy developed herein extends to other trace constituents including potential vorticity (Zapotocny et al. 1996; Egger 1999). Ideally, numerical accuracies concerning reversibility are optimized when the bias vanishes, the random component is minimal, and the distribution of differences equilibrates with time. Equilibration of the distribution of differences indicates that the error structure of a model is not interacting with the true state, thus generating bias functions with temporal dependence by virtue of nonlinearity. The strategy can also be extended to assess the relative merits of different numerical algorithms and resolutions within and among different models; for example, centered differences, forward differences, combination of different numerical schemes, and combination of different schemes with different resolutions etc. CCM2 and CCM3 with their capabilities for Eulerian spectral and semi-Lagrangian methods and capabilities for different resolutions and parameterizations are well suited for such experimental comparisons. The ready availability of these models has benefited efforts in development of UW isentropic models.

10. Summary

The application of the strategy developed in this study permits a statistical assessment of the impact of bias and random numerical errors and/or inconsistencies on thermodynamic and hydrologic processes that develop within the three categories of complex nonlinear weather and climate prediction models noted by von Neumann (1960).

As emphasized, the accurate simulation of the atmosphere's hydrologic cycle and reversible isentropic processes are crucial to the successful prediction of weather and climate. The inability to conserve appropriately both θ and θ_e during long-range transport limits the accuracies of weather and climate predictions.

The results from this study establish that both the bias and rms differences for θ_e and $t\theta_e$ in the simulation of moist reversible isentropic processes are markedly greater in the standard CCM3 and all follow-on CCM3/2 simulations than in the UW θ–σ model. Serious bias and rms differences due to numerical inconsistencies in the simulation of θ_e and $t\theta_e$ were identified in the standard CCM3 simulations. Detailed analysis of the CCM3 statistics revealed that the largest differences of θ_e and $t\theta_e$ were associated with inaccuracies in the semi-Lagrangian transport of $t\theta_e$. They stemmed from the use of Hermite cubic polynomials and overly constrained boundary conditions for layers adjacent to and near the upper and lower boundaries and the lack of continuity of first-and higher-order derivatives at the arrival levels of departure points. Because the source of the difficulties rests with $t\theta_e$ and the condition that water vapor is minimal in the upper layers, the actual simulation of θ_e in the stratosphere being determined primarily by CCM3's Eulerian spectral numerics in simulating θ is free of the implied error from the large differences. The follow-on experiments revealed that the rms differences utilizing CCM3 semi-Lagrangian numerics are less than either all-Eulerian spectral or mixed Eulerian spectral semi-Lagrangian numerics. However, the all–semi-Lagrangian numerics produced physically unrealistic mean equivalent potential temperatures at the 33 and 64H layers just as in the standard CCM3 simulation and large negative outliers with magnitudes in excess of -40 K were evident in the logarithmic profile for the relative frequency distribution.

The striking evidence of the accuracies of simulating reversible processes by the UW θ–σ model is provided by the visual inspection of Fig.5. First of all, note in Figs. 5b and 5d that actual values at day 10 range from -7 to 7 K for the UW θ–σ model and from -43 to 120 K for CCM3. In Figs. 5c and 5d, the UW θ–σ model frequency distributions for all four time periods are nearly coincident within a class interval that is one-tenth of the interval in Figs. 5a and 5b for CCM3 and the maximum frequency of occurrence is centered at zero indicating zero bias. The near invariance of the relative frequency distribution indicates the distributions of rounding and truncation errors are minimal and random throughout the domain and that the error distribution is equilibrating. Thus an optimum result given by utilizing isentropic coordinates to simulate reversibility associated with dry and moist adiabatic processes has been realized.

In conclusion, the UW θ–σ model enjoys a high level of accuracy for explicit simulations of thermodynamic processes including reversibility, condensation/evaporation processes, and long-range transport of entropy, water vapor, and cloud water/ice.

Acknowledgments. This research was supported by NASA under Grant NAG5-4398 and the Department of Energy under Grant DE-FG02-92ER61439 and IBM through the donation of an IBM RS/6000 for climate model development and analysis. The authors gratefully acknowledge the assistance of Judy Mohr in preparation of the manuscript. Computations were performed locally on the IBM RS/6000 and at the National Energy Research Scientific Computing Center (NERSC) and the NASA Center for Computational Sciences (NCCS).

REFERENCES

Acker, T. I., L. E. Buja, J. M. Rosinski, and J. E. Treiesdale, 1996: User's Guide to NCAR CCM3. NCAR Tech. Note NCAR/TN-421-1A, 210 pp.

Anderson, R. L., and T. A. Bancroft, 1952: *Statistical Theory in Research.* McGraw-Hill, 399 pp.

Arakawa, A., and V. Lamb, 1977: Computational design of the basic dynamical processes of the UCLA general circulation model. *Methods in Computational Physics,* J. Chang, Ed., Vol. 17, Academic Press, 173–265.

Atkinson, K. E., 1978: *An Introduction to Numerical Analysis.* John Wiley and Sons, 587 pp.

Boer, G. J., and Coauthors, 1991: An intercomparison of the climates simulated by 14 atmospheric general circulation models. WCRP Rep. 58, WMO/TD 425, 165 pp. [Available from World Meteorological Organization, 7 bis Avenue de la Paix, CP 2300, 1211 Geneva 2, Switzerland.]

——, and Coauthors, 1992: Some results from an intercomparison of the climates simulated by 14 atmospheric general circulation models. *J. Geophys. Res.,* **97,** 12 771–12 786.

Bolton, D., 1980: The computation of equivalent potential temperature. *Mon. Wea. Rev.,* **108,** 1046–1053.

Box, G. E. P., W. G. Hunter, and J. P. S. Hunter, 1978: *Statistics for Experimenters: An Introduction to Design, Data Analysis and Model Building.* John Wiley and Sons, 653 pp.

Dutton, J. A., 1976: *The Ceaseless Wind.* McGraw-Hill, 579 pp.

Egger, J., 1999: Numerical generation of entropies. *Mon. Wea. Rev.,* **127,** 2211–2216.

Greenspan, D., 1971: *Introduction to Numerical Analysis and Applications.* Markham, 182 pp.

Hack, J. J., B. A. Boville, B. P. Briegleb, J. T. Kiehl, P. J. Rasch, and D. L. Williamson, 1993: Description of the NCAR Community Climate Model (CCM2). NCAR Tech. Note NCAR/TN-382+STR, 108 pp.

Held, I. M., and M. J. Suarez, 1994: A proposal for the intercomparison of the dynamical cores of atmospheric general circulation models. *Bull. Amer. Meteor. Soc.,* **75,** 1825–1830.

Hughes, T. J. R., L. P. Franca, and M. Mallet, 1986: A new finite element formulation for computational fluid dynamics: I. Symmetric forms of the compressible Euler and Navier–Stokes equations and the second law of thermodynamics. *Comput. Methods Appl. Mech. Eng.,* **V54,** 223–234.

Johnson, D. R., 1980: A generalized transport equation for use with meteorological coordinate systems. *Mon. Wea. Rev.,* **108,** 733–745.

——, 1989: The forcing and maintenance of global monsoonal circulations: An isentropic analysis. Advances in Geophysics, Vol. 31, Academic Press, 43–316.

——, 1997: ''General coldness of climate models'' and the second law: Implications for modeling the earth system. *J. Climate,* **10,** 2826–2846.

——, 2000: *Entropy, the Lorenz Energy Cycle and Climate.* Vol. 70, *General Circulation Modeling: Past, Present and Future.* Academic Press, 807 pp.

——, and W. K. Downey, 1975: Azimuthally-averaged transport and the budget equations for storms: Quasi-Lagrangian diagnostics 1. *Mon. Wea. Rev.,* **103,** 967–979.

——, T. H. Zapotocny, F. M. Reames, B. J. Wolf, and R. B. Pierce, 1993: A comparison of simulated precipitation by hybrid isentropic-sigma and sigma models. *Mon. Wea. Rev.,* **121,** 2088–2114.

Kiehl, J. T., J. J. Hack, G. B. Bonan, B. A. Boville, B. P. Briegleb, D. L. Williamson, and P. J. Rasch, 1996: Description of the NCAR Community Climate Model (CCM3). NCAR Tech. Note NCAR/TN420+STR, 152 pp. [Available from UCAR Communications, P.O. Box 3000, Boulder, CO 80307.]

Lax, P. D., 1971: Shock waves, and entropy. *Contributions to Nonlinear Functional Analysis,* E. Zarantonello, Ed., Academic Press, 603–634.

Leslie, L. M., and G. S. Dietachmeyer, 1997: Comparing schemes for integrating the Euler equations. *Mon. Wea. Rev.,* **125,** 1687–1691.

Lin, S.-J., and R. B. Rood, 1996: Multidimensional flux-form semi-Lagrangian transport schemes. *Mon. Wea. Rev.,* **124,** 2046–2070.

Merriam, M. L., 1989: An entropy-based approach to nonlinear stability. NASA Tech. Memo. 101086, 144 pp. [Available from Ames Research Center, Moffett Field, CA 94035.]

Navarra, A., W. F. Stern, and K. Myjakoda, 1994: Reduction of the Gibbs oscillation in spectral model simulations. *J. Climate,* **7,** 1169–1183.

Pellerin, P., R. Laprise, and I. Zawadzki, 1995: The performance of a semi-Lagrangian transport scheme for the advection–condensation problem. *Mon. Wea. Rev.,* **123,** 3318–3330.

Pierce, R. B., D. R. Johnson, F. M. Reames, T. H. Zapotocny, and B. J. Wolf, 1991: Numerical investigations with a hybrid isentropic-sigma model. Part I: Normal model characteristics. *J. Atmos. Sci.,* **48,** 2005–2024.

Rasch, P. J., and D. L. Williamson, 1990a: On shape-preserving interpolation and semi-Lagrangian transport. *SIAM J. Sci. Stat. Comput.,* **11,** 656–697.

——, and ——, 1990b: Computational aspects of moisture transport in global models of the atmosphere. *Quart. J. Roy. Meteor. Soc.,* **116,** 1071–1090.

——, and ——, 1991: The sensitivity of a general circulation model climate to the moisture transport formulation. *J. Geophys. Res.,* **96,** 13 123–13 137.

Reames, F., and T. H. Zapotocny, 1999: Inert trace constituent transport in sigma and hybrid isentropic-sigma models. Part II: Twelve semi-Lagrangian algorithms. *Mon. Wea. Rev.,* **127,** 188–200.

Roads, J. O., S.-C. Chen, J. Kao, D. Langley, and G. Glatzmaier, 1992: Global aspects of the Los Alamos general circulation model hydrologic cycle. *J. Geophys. Res.,* **97,** 10 051–10 068.

Schubert, S. D., R. B. Rood, and J. Pfaendtner, 1993: An assimilated dataset for earth science applications. *Bull. Amer. Meteor. Soc.,* **74,** 2331–2342.

Sommerfeld, A., 1964: *Thermodynamics and Statistical Mechanics: Lectures on Theoretical Physics.* Vol. 5. Academic Press, 401 pp.

von Neumann, J., 1943: Theory of shock waves. *John von Neumann, Collected Works.* 2d ed. A. H. Taub, Ed., Pergammon Press, 178–202.

——, 1960: Some remarks on the problem of forecasting climatic fluctuations. *Dynamics of Climate,* R. L. Pfeffer, Ed., Pergamon, 9–11.

Whittaker, T. M., and R. A. Petersen, 1977: Objective cross-sectional analyses incorporating thermal enhancement of the observed winds. *Mon. Wea. Rev.,* **105,** 147–153.

Williamson, D. L., and P. J. Rasch, 1989: Two-dimensional semi-Lagrangian transport with shape preserving interpolation. *Mon. Wea. Rev.,* **117,** 102–129.

——, and J. G. Olson, 1994: Climate simulations with a semi-Lagrangian version of the NCAR Community Climate Model. *Mon. Wea. Rev.,* **122,** 1594–1610.

——, J. T. Kiehl, and J. J. Hack, 1995: Climate sensitivity of the NCAR Community Climate Model (CCM2) to horizontal resolution. *Climate Dyn.,* **11,** 377–397.

——, J. G. Olson, and B. A. Boville, 1998: A comparison of semi-Lagrangian and Eulerian tropical climate simulations. *Mon. Wea. Rev.,* **126,** 1001–1012.

Zapotocny, T. H., D. R. Johnson, and F. R. Reames, 1994: Development and initial test of the University of Wisconsin global isentropic–sigma model. *Mon. Wea. Rev.,* **122,** 2160–2178.

——, A. J. Lenzen, D. R. Johnson, F. M. Reames, P. A. Politowicz, and T. K. Schaack, 1996: Joint distributions of potential vorticity and inert trace constituent in CCM2 and UW θ–σ model simulations. *Geophy. Res. Lett.,* **23,** 2525–2528.

——, ——, ——, ——, and T. K. Schaack, 1997a: A comparison of inert trace constituent transport between the University of Wisconsin isentropic–sigma model and the NCAR Community Climate Model. *Mon. Wea. Rev.,* **125,** 120–142.

——, D. R. Johnson, T. K. Schaack, A. J. Lenzen, F. M. Reames, P. A. Politowicz, and Z. Yuan, 1997b: Simulations of tropospheric joint distributions in the UW θ–σ model and CCM2. *Geophys. Res. Lett.,* **24,** 865–868.